Joana Marques Cerdeira

Bachelor in Micro and Nanotechnology Engineering Sciences

Study of Thermoelectric Properties of Indium Silicon Oxide Thin Films

Dissertation submitted in partial fulfillment
of the requirements for the degree of

Master of Science in
Micro and Nanotechnology Engineering

Adviser: Dr. Arokia Nathan, Full Professor,
University of Cambridge

Co-adviser: Dr. Rodrigo Martins, Full Professor, Faculty of Sciences
and Technology, NOVA University of Lisbon

Examination Committee

Chairperson: Dr. Hugo Manuel Brito Águas, Assistant Professor, FCT-UNL
Raporteurs: Dr. Luís Miguel Nunes Pereira, Associate Professor, FCT-UNL
Dr. Rodrigo Ferrão de Paiva Martins, Full Professor, FCT-UNL

FACULDADE DE
CIÊNCIAS E TECNOLOGIA
UNIVERSIDADE NOVA DE LISBOA

September, 2017

Study of Thermoelectric Properties of Indium Silicon Oxide Thin Films

Copyright © Joana Marques Cerdeira, Faculty of Sciences and Technology, NOVA University Lisbon.
The Faculty of Sciences and Technology and the NOVA University Lisbon have the right, perpetual and without geographical boundaries, to file and publish this dissertation through printed copies reproduced on paper or on digital form, or by any other means known or that may be invented, and to disseminate through scientific repositories and admit its copying and distribution for non-commercial, educational or research purposes, as long as credit is given to the author and editor.

"Somewhere, something incredible is waiting to be known."

Carl Sagan

Acknowledgements

Firstly, I would like to thank Professor Rodrigo Martins and Professor Elvira Fortunato for the work and effort put in the creation and continuous improvement of the course of Micro and Nanotechnology Engineering.

I would also like to thank all the people involved in the BET-EU project for the opportunity to develop my Master dissertation abroad. This was one of the best experiences I have ever had and truly enriched me in a personal and professional way. Again, I would like to thank Professor Rodrigo Martins for the support given during this dissertation as my co-adviser. To Professor Pedro Barquinha for the help with the boarding passes and finally a special thank to Diana Gaspar for all the work in finding us a wonderful house near CAPE and also in the preparation and help provided throughout this adventure.

To my advisor in University of Cambridge, Professor Arokia Nathan for the assistance and guidance given during the project. To Constantinos Tsangarides for all the help provided when I most needed. Thank you for the introduction and the insight in the thermoelectrics field, the wise advices, and the help in the fabrication and characterisation of the first samples.

To all the HGL group, especially to Guangyu Yao for helping me with the thin films and electrodes deposition, and to Hanbin Ma for the advices and help given in the resistivity measurements. Finally, last but not least, to Choi for helping me in the laboratory and for the conversations at the end of the day.

I would like to thank Professor Joana Pinto, Rita Branquinho, Daniela Nunes, and Tomás Calmeiro for the assistance provided on the remaining characterisation of my samples in CENIMAT.

To Beatriz Coelho and Mónica Machado for all the jokes, conversations, and advices throughout these six years. The best moments I had were with you by my side. Beatriz, your hard-work and the commitment you apply to every project is inspiring. You are one of my best friends and one of the funniest people I have had the pleasure to meet. Mónica, you have a lot of potential and I know one day your ideas will stop being ideas and will start to be interesting projects. Never give up!

To all my colleagues with whom I had the pleasure to meet and work all these years. This course is full of interesting and hard-working people. Keep the good work.

To Tiago Gonçalves, Jorge Emídio, Cátia Figueiredo, Vasco Santos, and Miguel Cunha with whom I enjoyed to work with in iNOVAfuture. Your passion to continuously improve this project, which is getting more visibility every year, truly inspired me and I am glad I had the chance to get to know you better.

To all the group that never missed one day of work and with whom I laughed so much at the open-space.

To Ana Beaumont, Shiv Bhudia and João Crespo for the best housemates I could ask for. Thank you all for the funniest moments, deep conversations, and good dishes. I never had the chance to cook the duck rice but who knows, maybe one day.

To my longtime friends: Ana, Sofia, Vera, Eunice, Giovanny and Diogo. I am so lucky to say I have the best friends ever with whom I can count on whenever I need. With you I have laughed, cried, and shared good moments all these years and I hope our friendship last many more.

To my parents who have supported and invested in me all these years so I could have this opportunity and a good formation. For me you are the best parents in the world. Thank you so much for everything!

To my dear sister, thank you for listening me when I most needed and for the support. With you I have learnt so many, specially not to be afraid to embrace a new challenge in our life and to give our best. I could not ask for a better sister and I am so proud of you and what you have accomplished. I hope this new adventure will bring you more opportunities.

Finally, to Tiago with whom I hope to share many more laughs and good moments like the ones we have been sharing so far. Thank you for inviting me for lunch that day. I hope I can continue to annoy you.

Abstract

Thermoelectric devices, which convert heat into electricity, are regarded as an environmentally friendly alternative to fossil fuels used as the main resource for energy production. In the last few decades, transparent oxide semiconductors and conductors, namely Indium oxide-based materials, have been studied and applied in thin film transistors and solar cells. Nevertheless, this group of materials has also been studied for thermoelectric applications.

In this dissertation, amorphous Indium silicon oxide (ISO) thin films were sputtered at room temperature on glass substrate, under different oxygen contents in the argon and oxygen mixture.

The thermoelectric properties were evaluated as a function of deposition conditions and post-deposition annealing parameters (temperature and time). These properties were analysed and correlated with respective structural, morphological, optical, and electrical properties. For films deposited with no oxygen and annealed at 300 ºC for 24 h, the Seebeck coefficient and electrical resistivity at room temperature were $-68.6\,\mu\mathrm{V\,K^{-1}}$ and $4.7\times10^{-2}\,\Omega\,\mathrm{cm}$, respectively. Thin films deposited at higher oxygen percentages showed, in turn, very low conductivity values not being possible to measure the Seebeck coefficient. The maximum power factor achieved was $10\,\mu\mathrm{W\,m^{-1}\,K^{-2}}$ for the aforementioned annealing conditions. A simultaneous increase of the Seebeck coefficient and electrical conductivity was also observed, mainly due to scattering mechanisms which enhanced the Seebeck coefficient.

Although ISO thin films properties present a good stability when submitted to different post-deposition conditions, further studies need to be performed in order to optimise the thermoelectric properties and hence the power factor.

Keywords: Indium silicon oxide, Seebeck coefficient, amorphous thin films, annealing, reactive sputtering, oxygen percentage

Resumo

Os dispositivos termoelétricos, que convertem calor em eletricidade, são considerados como uma alternativa ecológica aos combustíveis fósseis utilizados como principal recurso para a produção de energia. Nas últimas décadas, os semicondutores e condutores óxidos transparentes, nomeadamente os materiais à base de óxido de índio, têm sido estudados e aplicados em transístores de filme fino e células solares. No entanto, esta classe de materiais também tem sido estudada para aplicações termoelétricas.

Nesta dissertação, filmes finos amorfos de óxido de índio e silício (ISO) foram pulverizados à temperatura ambiente em substratos de vidro, sob diferentes concentrações de oxigénio na mistura de árgon e oxigénio.

As propriedades termoelétricas foram avaliadas em função das condições de deposição e dos parâmteros de tratamento térmico (temperatura e tempo). Estas propriedades foram analisadas e correlacionadas com as respectivas propriedades estruturais, morfológicas, óticas e elétricas. Para filmes depositadas na ausência de oxigénio e recozidos a 300 ºC durante 24 h, o coeficiente de Seebeck e a resistividade elétrica à temperatura ambiente foram $-68.6\,\mu\mathrm{V\,K^{-1}}$ e $4.7\times10^{-2}\,\Omega\,\mathrm{cm}$, respetivamente. Porém, os filmes finos depositados com percentagens de oxigénio mais elevadas apresentaram, por sua vez, valores de condutividade muito baixos não sendo possível medir o coeficiente de Seebeck. O fator de potência máximo alcançado foi de $10\,\mu\mathrm{W\,m^{-1}\,K^{-2}}$ para as condições de recozimento acima mencionadas. Um aumento simultâneo do coeficiente de Seebeck e da condutividade elétrica foi observado, devendo-se principalmente aos mecanimos de dispersão que melhoraram o coeficiente de Seebeck.

Embora os filmes finos de ISO apresentem boa estabilidade quando submetidos a diferentes condições de pós-deposição, é necessário realizar mais estudos para otimizar as propriedades termoelétricas e consequentemente o fator de potência.

Palavras-chave: Óxido de índio e silício, coeficiente de Seebeck, filmes finos amorfos, recozimento, pulverização catódica reativa, percentagem de oxigénio

Contents

List of Figures xv

List of Tables xvii

Symbols xix

Acronyms xxi

Motivation and Objectives xxiii

1 Introduction **1**
- 1.1 Thermoelectric effects 1
  - 1.1.1 Seebeck Effect 1
- 1.2 Thermoelectric properties 3
  - 1.2.1 Electrical conductivity 3
  - 1.2.2 Seebeck coefficient 4
  - 1.2.3 Thermal conductivity 4
  - 1.2.4 Figure of Merit 4
- 1.3 Thermoelectric materials 5
  - 1.3.1 Oxide-based materials 6

2 Materials, processing, and characterisation **9**
- 2.1 Thin-film deposition 9
- 2.2 Electrodes deposition 9
- 2.3 Characterisation techniques 10

3 Results and Discussion **13**
- 3.1 Sputtering atmosphere influence on the growth rate 13
- 3.2 Characterisation of ISO thin-films 15
  - 3.2.1 Structural characterisation 15
  - 3.2.2 Morphological characterisation 17
  - 3.2.3 Compositional analysis 19
  - 3.2.4 Optical characterisation 20
  - 3.2.5 Electrical characterisation 23
  - 3.2.6 Thermoelectric characterisation 26

4 Conclusions and Future Perspectives **31**

Bibliography **33**

A Thermoelectric effects 39

B Structural characterisation 41

C Morphological characterisation 43

D Optical characterisation 45

E Relative Seebeck coefficient determination 47

List of Figures

1.1 Development of an electrical potential as a result of a temperature gradient. Negative charge carriers flow from the hot side to the cold side, inducing an electric field, E. Adapted from [11] . . . 1

1.2 Semiconductor thermocouple for power generation. The resistance represents the load connected to the thermocouple. . . . 2

1.3 Dependence of the Seebeck coefficient, electrical conductivity, power factor, and thermal conductivity on carrier concentration. From [13] . . . 3

2.1 Demonstration of the 2-point geometry used for thermoelectric measurements of ISO thin films. Two copper pins at a distance of 12 mm of each other on top of Mo electrodes are used for acquisition of thermoelectric voltage. The two K-type thermocouples are placed a few mm from the copper pins for temperature readings. 11

3.1 Dependence of the growth rate on %O_2 present in the sputtering atmosphere. . . . 14

3.2 Structure of ISO thin films for (a) different %O_2 annealed at 150 ºC for 12 h and (b) for different annealing periods at 300 ºC. . . . 15

3.3 SEM images of films deposited under different oxygen contents and annealed at 300 ºC for 24 h: (a) 0 %, (b) 3 %, and (c) 17 %. . . . 17

3.4 AFM images of thin films sputtered at different oxygen contents and annealed at 300 ºC for 24 h. . . . 18

3.5 Atomic concentration of silicon and indium for as-deposited ISO thin films. . . . 19

3.6 Transmittance of ISO thin films deposited under sputtering atmospheres with different %O_2 and annealed a) at 150 ºC and b) at 300 ºC for different periods. . . . 20

3.7 Optical bandgap determined by Tauc plot for (a) films annealed at 150 ºC for 12 h, and for (b) films deposited under inert atmosphere and annealed at 300 ºC for different periods. The curve for as-deposited thin films is given for reference. . . . 22

3.8 Electrical resistivity for (a) different annealing temperatures and (b) different periods (at 300 ºC) of ISO thin films deposited under different O_2 content in the sputtering atmosphere. . . . 23

3.9 Illustration of ISO thin films constitution, where the grey circles are conductors and the white circles are insulators. The incorporation of Si supress the formation of oxygen vacancies (V_O). From [39] . . . 24

3.10 Influence of (a) annealing temperature and (b) annealing period on resistivity, mobility, and carrier concentration for thin films deposited under 0 % of O_2. . . . 25

3.11 Relation between electrical resistivity and Seebeck coefficient for different (a) annealing temperatures and (b) annealing periods of films deposited with 0% O_2. The absolute Seebeck coefficient is given in module. . . . 27

3.12 Power Factor for (a) different annealing temperatures and (b) different annealing times of films deposited under 0% O_2. 29

A.1 Illustration of a Peltier module. From [75] 40

B.1 Structure of ISO thin films annealed at different temperatures a) $\%O_2$ = 0%, b) $\%O_2$ = 3% and at different annealing times c) $\%O_2$ = 3%, d) $\%O_2$ = 17% 41

C.1 Influence of different annealing temperatures on surface morphology for films deposited with (a) 0 % and (d) 17 % of $\%O_2$ and annealed at (b), (e) 150 ºC and (c), (f) 300 ºC. The SEM images for films deposited under 3 % of oxygen showed very similar results to films deposited under 17 %. 43

C.2 AFM images for (a)-(c) as-deposited and (d)-(f) annealed at 150 ºC ISO thin films deposited under different sputtering gas compositions. 44

D.1 Transmittance for films prepared with $\%O_2$ of (a) 3 % and (b) 17 % and annealed at 300 ºC for different periods. The inset explores the difference between each curve. . 45

D.2 Absorbance for films prepared with different $\%O_2$ of (a) 0 %, (b) 3%, and (c) 17 % and annealed at 300 ºC for different periods. Thin films with 3 % and 17 % of oxygen used during deposition have the same optical absorbance. 46

E.1 Slope method for determination of the relative Seebeck coefficient. 47

List of Tables

3.1 Roughness variation for thin films annealed at different temperatures and times. . . 19
3.2 Optical bandgap for ISO thin films annealed at different conditions. 22
3.3 Electric characteristics of thin films deposited with 3% and 17% of oxygen and annealed at 300 ºC for different times. 25
3.4 Comparison of thermoelectric properties of ISO thin films with other amorphous oxides published in literature. 30

Symbols

$\%O_2$	Percentage of oxygen content in the sputtering gas mixture
A	Absorbance
B	Full width at half maximum
D	Crystallite size
E_F	Fermi Energy
E_{opt}	Optical bandgap
e	Elementary charge of an electron
h	Plack's constant
I	Electric current
k_B	Boltzmann constant
m_e	Electron rest mass
m^*	Charge carrier effective mass
n	Carrier concentration
q	Rate of heating or cooling
r	Scattering exponent
r_{RMS}	Root-mean-square roughness
S	Seebeck coefficient
S_{AB}	Differential Seebeck coefficient
T	Absolute temperature
T_A	Annealing temperature
ΔT	Temperature gradient

V Voltage

V_O Oxygen vacancy

α Absorption coefficient

λ Thermal conductivity

λ_e Electronic thermal conductivity

λ_L Lattice thermal conductivity

μ Carrier mobility

π_{AB} Differential Peltier coefficient

ρ Electrical resistivity

σ Electrical conductivity

τ Relaxation time

τ_{AB} Differential Thomson coefficient

θ Bragg diffraction angle

v Photon's frequency

Acronyms

AFM	Atomic force microscopy
AZO	Aluminum-doped zinc oxide
EDS	Energy-dispersive X-ray spectroscopy
emf	Electromotive force
FPP	Four-point probe
IGZO	Indium gallium zinc oxide
IPA	Isopropyl alcohol
ISO	Indium silicon oxide
ITiO	Indium titanium oxide
ITO	Indium tin oxide
IWO	Indium tungsten oxide
IZO	Indium zinc oxide
IZTO	Indium zinc tin oxide
PF	Power Factor
SEM	Scanning electron microscopy
TCO	Transparent conducting oxide
TFT	Thin-film transistor
TSO	Transparent semiconducting oxide
XRD	X-ray diffraction
ZnO	Zinc oxide

Motivation and Objectives

Over the past few decades, society's demands, specially in developed countries, have relied mostly on fossil fuels as the main resources for energy production [1]. With the fast growth of consumerism and, consequently, industrialisation and urbanisation, predictions of the fossil fuels reserves depletion started to converge to a near future alongside with negative environmental, economical, and social impacts.

In order to meet the goals proposed on the 2030 Agenda for Sustainable Development [2], more energy directives are being set to reduce governments dependency on non-renewable sources. For instance, Europe intends to achieve 20% of renewable energy to satisfy its energy needs by 2020. By 2030, Europe proposes the achievement of a new renewable energy target of 27% according to EU's energy and climate goals for that year [3].

The use of renewable energy has not only been increasing over the past few years, but has also become an excellent alternative since it can promote new investments, technology innovation, and decreasing costs [1]. In fact, the primary energy supplied by renewables reached 9.7% in 2016. With respect to electricity, 23.8% of all electricity generated in that year was provided by renewable resources, where hydropower represented the largest share of renewable generation [1].

Renewable energy resources can be divided by power capacity into hydropower and ocean, wind, solar photovoltaic, bioenergy, and geothermal.

Nevertheless, heat is also one abundant source of energy. Most of the energy produced is lost as waste heat, for example in industrial processes and in exhaust from auto-mobiles [4]. As a solution, thermoelectric devices can be implemented to overcome this problem since they rely on the phenomenon of converting heat into clean electricity without moving parts. For instance, these devices can be applied to wearables as batteries, as well as cooling for small scale refrigeration. The latter application is accomplished by using the reverse thermoelectric effect. One simple and well-known application is a thermocouple used as a temperature sensor, constituted by two different materials.

However, a thermoelectric module, which is constituted by several thermocouples, is available commercially in the bulk form. This can represent a disadvantage to new electronic applications which rely most on thin-film materials.

Transparent conducting oxides (TCOs) are a class of materials with particular properties, such as optical transparency and high electrical conductivity. The intensive research has allowed the application of TCOs in solar cells as electrodes, in liquid crystal displays (LCDs), among other applications. Additionally, applications in transparent thin film transistors (TFTs) are also possible, although transparent semiconducting oxides (TSOs) are used in turn [5]. These oxides can be deposited as thin-films, which constitute an advantage since it allows the implementation in small and thin applications.

Semiconductors, such as bismuth telluride (BiTe), lead telluride (PbTe), and silicon germanium (SiGe) are usually the preferred material for thermoelements implementation.

Nevertheless, some oxides have been studied for applications in thermoelectrics, which are example the indium oxide-based materials, motivated by the challenge to increase the performance of thermoelectric materials and to further expand the range of thermoelectric applications. In addition, these oxides can be deposited as transparent thin-films.

Indium silicon oxide (ISO) is an example of that group of materials, and it is mostly studied for applications in thin film transistors and as transparent electrodes for solar cells [6, 7]. However, its thermoelectric properties have never been studied, for the best of our knowledge. Therefore, the main purpose of this thesis is the preparation of ISO thin films, based on different deposition conditions and post-deposition parameters, and the study of the effect of these configurations on its properties, namely the thermoelectric properties.

This study also intends to evaluate the performance of ISO as a thermoelectric material at room temperature, to conclude which configuration allows the best performance, and to suggest some future work in order to optimise these properties.

Chapter 1

Introduction

Environmental problems such as the global warming and depletion of energy resources serve as motivation to discover new environmental friendly alternatives. It was soon recognised that heat could be used as a source for electricity generation, and cooling could be realised by passing current through a material. These applications were only possible owing to the discover of thermoelectric effects.

Thermoelectric energy converters are cleaner alternatives without moving components, fact that is proved by the absence of toxic residuals. However, the efficiency of thermoelectric devices remain low, being impossible for the moment to surpass the well-establish applications for energy conversion [8]. The materials employed in thermoelectric devices are one of the main reasons for low efficiency. Therefore, this subject requires further research so the efficiency can be improved.

In order to fully understand the thermoelectrics field, the following sections introduce the fundamentals of thermoelectric effects, thermoelectric transport properties, and the attention that has been given to oxide thermoelectric materials.

1.1 Thermoelectric effects

1.1.1 Seebeck Effect

The beginning of thermoelectrics back to 1821 when Thomas Johann Seebeck discovered the first thermoelectric effect, which would later be known as the Seebeck effect [9]. In figure 1.1 this effect is illustrated, where an electrical potential is generated when a temperature gradient is applied to a material [10]. As a consequence, the electronic charge carriers move from the hot side (energetic electrons have long mean free path) to the cold side (electrons have short mean free path), resulting in a current flow [8, 10].

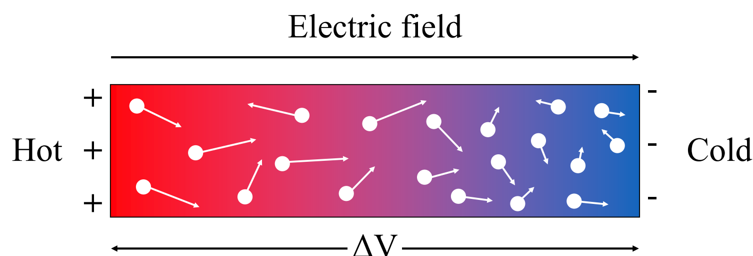

Figure 1.1: Development of an electrical potential as a result of a temperature gradient. Negative charge carriers flow from the hot side to the cold side, inducing an electric field, E. Adapted from [11]

One simple way to demonstrate this effect is by using a thermocouple, which is composed of wires of two different conductors, usually metals or metal alloys, electrically connected in series and thermally in parallel. When the junction between the two metals is heated, an open electromotive force (emf) is generated (detected when there is a voltmeter connected) [12]. This thermoelectric voltage is proportional to the difference between the temperature at the thermocouple junction and at the connections to the meter:

$$S_{ab} = \frac{V}{\Delta T} \tag{1.1}$$

where ΔT is the temperature difference between the two junctions, V is the electrical potential that appears at the two ends, and S_{ab} is the differential Seebeck coefficient under open circuit conditions in V/K. The Seebeck coefficient can also be referred to as thermoelectric power, thermopower or thermal emf and is positive if a current drives from the hot side to the cold side [9].

In spite of the fact that metal thermocouples are commonly used for temperature measurement and as sensors, it was only with the use of semiconductors as thermoelements that efficiency started to raise. Semiconductors thermocouples, as depicted in figure 1.2, are common nowadays and commercial applications can be found for cooling and power generation purposes [9].

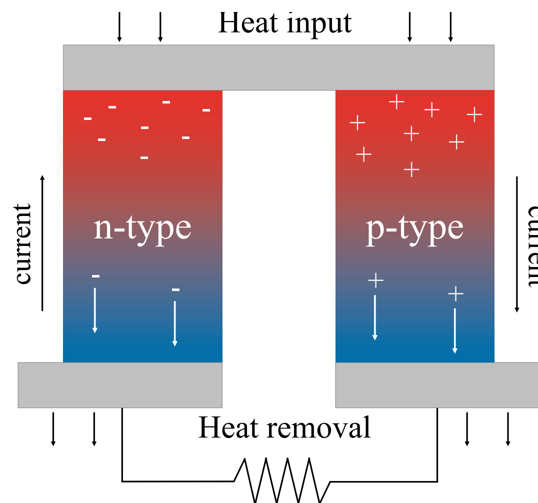

Figure 1.2: Semiconductor thermocouple for power generation. The resistance represents the load connected to the thermocouple.

With the latter type of thermocouples, material's properties and geometry can be tailored to meet the application requirements. In addition, the Seebeck coefficient is higher for semiconductors (hundreds of microvolts per degree) than for metals (tens of microvolts per degree).

As observed in figure 1.2, there are two legs or thermoelements: one n-type and one p-type. These thermoelements are usually ingot-shaped pellets connected at one end with an electrically conducting metal strap and used in bulk devices.

The performance of a thermocouple takes into account the differential Seebeck coefficient, the thermal conduction and electrical resistance of the two thermoelements. These last two effects are irreversible and always accompany the thermoelectric phenomena [9].

After the discover of the Seebeck effect, two more were discovered (Peltier and Thomson effect) and are described in appendix A. In this work only the Seebeck effect was studied.

1.2 Thermoelectric properties

1.2.1 Electrical conductivity

The electrical resistivity, ρ, is one of the most important parameters that characterise a material. The inverse of ρ is the electrical conductivity, σ. As shown in figure 1.3, both the Seebeck coefficient and the electrical conductivity are functions of carrier concentration, n. While the electrical conductivity increases with n the opposite occurs for the Seebeck coefficient. As it will be explained later on, the product of the square of the Seebeck coefficient with the electrical conductivity, the power factor PF, ($S^2\sigma$) maximizes at a carrier concentration of around 10^{19} cm^{-3}, typical of semiconductors [12].

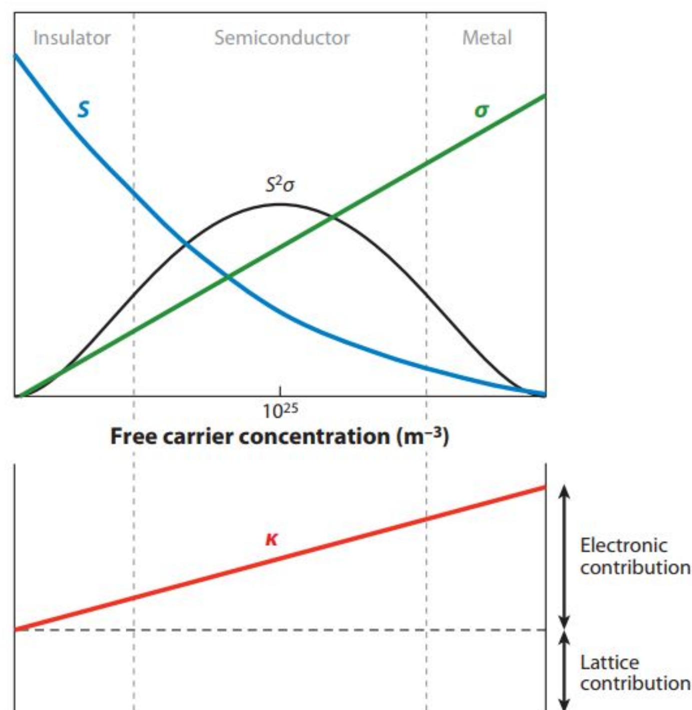

Figure 1.3: Dependence of the Seebeck coefficient, electrical conductivity, power factor, and thermal conductivity on carrier concentration. From [13]

In a semiconductor, it is convenient to express the electrical conductivity by the following expression

$$\sigma = ne\mu \tag{1.2}$$

where n is the carrier concentration, μ is the carrier mobility, and e is the charge of unit carrier.

1.2.2 Seebeck coefficient

The Seebeck coefficient, S, is a fundamental electronic property, resulting from the presence of charge carriers and their motion. Phonons, interactions between charges, and magnetic moments affect this coefficient. Sometimes, the carrier's interactions can enhance the Seebeck coefficient [12].

The Seebeck coefficient, S, is defined using the following Mott formula, when the energy E equals the Fermi energy [14]:

$$\begin{aligned} S &= \frac{\pi^2}{3}\left(\frac{k_B^2 T}{e}\right)\left[\frac{\partial \ln\sigma(E)}{\partial E}\right]_{E=E_F} \\ &= \frac{\pi^2}{3}\left(\frac{k_B^2 T}{e}\right)\left[\frac{1}{n}\frac{\partial n(E)}{\partial E}+\frac{1}{\mu}\frac{\partial \mu(E)}{\partial E}\right]_{E=E_F} \end{aligned} \tag{1.3}$$

where e is the carrier charge, T is the temperature, k_{B} is the Boltzmann constant, $\sigma(E)$ is the energy dependent electrical conductivity, E_F is the Fermi energy, $n(E)$ is the energy dependent charge carrier concentration, and $\mu(E)$ is the energy dependent carrier mobility.

Equation 1.3 predicts the Seebeck coefficient reduction with increasing carrier concentration, as observed in figure 1.3.

1.2.3 Thermal conductivity

Charge carriers present in metals and semiconductors carry not only an electronic, but also a thermal component. Heat is also carried by thermal vibrations present in the structure of the materials [12]. The total thermal conductivity, λ, is the sum of the electronic component, λ_{e}, and the lattice component, λ_{L}, as expressed by:

$$\lambda = \lambda_{\mathrm{e}} + \lambda_{\mathrm{L}} \tag{1.4}$$

The electronic thermal conductivity, λ_{e}, is in turn determined by the Lorenz number, L ($2.44 \times 10^{-8}\,\mathrm{W\,\Omega\,K^{-2}}$), given by

$$L = \frac{\lambda_{\mathrm{e}}}{\sigma T} \tag{1.5}$$

For a semiconductor, the major contribution is given by the lattice thermal conductivity, being λ_{e} only 1/3 of the total thermal conductivity [12]. As it will be seen in the following section, it is convenient for thermal conductivity to be as small as possible in thermoelectrics. However, charge carrier concentration has also an effect on total thermal conductivity, as observed in figure 1.3. One solution for reduction of λ is by taking advantage of phonon scattering such as phonon-phonon scattering, phonon-defect scattering, and phonon-boundary scattering [15]. Lower thermal conductivities can be found in amorphous structures.

1.2.4 Figure of Merit

The concept of figure of merit, Z, is used to evaluate the efficiency of a thermoelectric material. This concepts combines three physical properties: the electrical conductivity, the Seebeck

coefficient, and the thermal conductivity. Nevertheless, it is common to express Z in dimensionless terms by multiplying it by the absolute temperature, T, in Kelvin once Z changes with temperature [12]:

$$ZT = \frac{S^2\sigma}{\lambda}T \tag{1.6}$$

where $S^2\sigma$ is the electrical power factor.

It was only in 1911, that Altenkirch related the thermocouple's performance to the thermoelectric properties. In order to achieve a higher performance, it would be needed a high differential Seebeck coefficient, high electrical conductivities of the two thermoelements, and low thermal conductivities [12].

As observed previously, it is difficult to obtain the desired ZT values, since all these properties depend on the carrier concentration in a reciprocal way, especially the electrical conductivity and Seebeck coefficient. From figure 1.3, the figure of merit optimizes at carrier concentrations typical of semiconductor materials [9]. In this work, it was not possible to determine the thermal conductivity, thus only the power factor was calculated.

1.3 Thermoelectric materials

Several materials can be regarded as thermoelectric materials: semiconductors, ceramics, oxides, and organics. As observed in figure 1.3, PF is higher for carrier concentrations characteristic of semiconductor materials. Hence, this class of materials are the most suitable for thermoelectric applications.

Only the materials with $ZT > 0.5$ are considered as thermoelectric materials. The conventional materials for commercial thermoelectric refrigeration consist of alloys based on bismuth in combinations with antimony, tellurium, and selenium, once they can be used at temperatures up to around 450 K [9]. For a long time, bismuth telluride (Bi_2Te_3) was the best thermoelectric material with ZT around one at room temperature [16]. Likewise, lead telluride and silicon germanium alloys are employed in commercial applications, for power generation, for temperatures up to around 850 K and up to 1300 K, respectively as they also present high ZT values [9].

In accordance with equation 1.6, it is difficult to improve all three transport coefficients simultaneously. As a result, thermoelectric materials are usually characterised by having low efficiency. It was due to intensive research and development on new classes of materials (skutterudites [17, 18], clathrates [19], and Half-Heusler alloys [20]), new structures (quantum wells [21, 22], quantum wires [23], quantum dots, and superlattices [24, 25]), and enhanced mechanisms for improvement of electronic transport that higher ZT began to be achieved by reducing the lattice thermal conductivity. Furthermore, these solutions pretend to substitute the bismuth-based alloys, once they are expensive and scarse [9, 26].

Overall, improved thermoelectric materials must fulfil the following parameters: enhanced thermoelectric performance, reduced lattice thermal conductivity, low cost, and environmentally friendly [9].

Some applications of thermoelectric devices can be found in appendix A.

1.3.1 Oxide-based materials

Oxide-based materials are not the suited thermoelectric candidates according to Ioffe's theory due to ionic bonding with a narrow band, when compared with covalent alloys. Furthermore, these materials present medium electrical conductivity (~100-200 $S\,cm^{-1}$) and high thermal conductivity (~3-10 $W\,m^{-1}\,K^{-1}$) which are also responsible for the low efficiency [27]. In addition, mobility and carrier concentration are lower than the covalent materials in two or three orders [28].

Most of the studied thermoelectric materials with comparable high performances are toxic, low in abundance, and their thermal or chemical stability are inferior. On the contrary, some oxide-based materials are characterised by possessing easy processing, low cost, high structural and chemical stability, and oxidation resistance. Although the ZT values are not high when compared to the well-established thermoelectric materials, these characteristics have led to a continuous study and development. A few examples are $SrTiO_3$ [29], ZnO [30], NiO [31], $Ca_3Co_4O_9$ [32], Na_xCoO_2 [33] and In_2O_3 [34]. Even though the best oxide materials studied for thermoelectric applications are *p*-type semiconductors, some *n*-type semiconductors are being studied as well since they have demonstrated to be good thermoelectric materials. For instance Al-doped ZnO (AZO) demonstrated a ZT ~0.3 at 1000 K [35].

In_2O_3-based materials are widely used as TCO owing to good electrical conductivity and its thermoelectric properties have been investigated. A few examples can be found in literature, where Ce-doped In_2O_3 has been reported as a promising candidate for thermoelectric application [27, 36]. The Zn dopant further improved its electrical properties, leading to a ZT of 0.4 at 1050 K [37]. Ge doping has also shown to be effective in improving thermoelectric properties with ZT exceeding 0.45 at 1273 K [34]. The study of other In_2O_3-based materials thermoelectric properties would be interesting, for instance the material introduced below. This is one of the main purposes of this work.

1.3.1.1 Indium Silicon Oxide

Indium oxide-based materials are known to exhibit good electrical conductivity, besides the fact to be transparent. Indium Silicon Oxide (ISO), for instance, is an *n*-type semiconductor whose thermoelectric characteristics have never been studied, for the best of our knowledge.

According to Maruyama *et al.* [38], ISO thin films prepared by radio frequency (RF) magnetron sputtering presented higher electrical conductivity and mobility than the ones showed for ITO thin films. Hence, this material has been studied for applications in thin film transistors and solar cells as a transparent conductor [6, 39, 40]. This oxide also presents good stable properties once it suppresses the formation of oxygen vacancies, as reported by Aikawa *et al.* [41], where the conductivity suffered very little change with oxygen partial pressure variation used during sputtering (10^{-2} $S\,cm^{-1}$ to 10^{2} $S\,cm^{-1}$), compared to indium titanium oxide (ITiO) and indium tungsten oxide (IWO). Lower resistivities were also reported with values bewteen 10^{-4} $\Omega\,cm$ to 10^{-3} $\Omega\,cm$ for sputtered ISO thin films (comparable to IZO and IZTO films) [6, 42, 43]. Moreover, ISO can be considered as a degenerated semiconductor with

n ranging from $10^{19}\,\mathrm{cm^{-3}}$ to $10^{20}\,\mathrm{cm^{-3}}$ [6, 40]. Finally, ISO can have mobilities up to $21\,\mathrm{cm^2\,V^{-1}\,s^{-1}}$, although lower than InTiO and IWO [6].

Chapter 2

Materials, processing, and characterisation

This work intends to study the influence of deposition conditions and post-deposition parameters on thermoelectric properties of ISO thin films. For this purpose, several characterisations were performed in order to understand and correlate ISO properties with its thermoelectric properties. This chapter covers the deposition process used for ISO thin films fabrication (based on previous work developed by The HGL group, University of Cambridge) and the thermal treatment applied to the films.

2.1 Thin-film deposition

Thin films of ISO were deposited by DC magnetron sputtering at 150 W using a sputtering system present in a Cluster Tool (MVSystems LLC). For this purpose, an ISO ceramic commercial target (90 wt.% In_2O_3 + 10 wt.% SiO_2) was used to investigate the impact of high SiO_2 content in the target composition on the thin films properties.

The depositions were performed for 30 min under reactive atmosphere with constant Ar (99.99% purity) flow rate of 50 sccm and different O_2 (99.99% purity) flow rates with configurations of 0, 1.5, and 10 sccm. The content of O_2 in the atmosphere mixture, designated henceforth by $\%O_2$, was calculated by equation. 2.1.

$$\%O_2 = \frac{O_2 \text{ flow}}{(Ar + O_2) \text{ flow}} \tag{2.1}$$

Sputter parameters such as deposition pressure and target to substrate distance were remained constant at 4×10^{-3} Torr and 12 cm, respectively. All the depositions were realized at room temperature.

Depending on the characterisation type, different substrates were used: glass substrate (Corning 70059 glass) previously cut into 4×4 cm squares, n-doped silicon wafer (100), and quartz glass. Prior to sputtering, all the substrates were ultrasonically cleaned in acetone and isopropyl alcohol (IPA), for 10 min, and 5 min, respectively. Then, the substrates were rinsed in de-ionized water and dried with N_2 flux.

2.2 Electrodes deposition

In order to characterise the thermoelectrical properties of the samples, Molybdenum (Mo) electrodes with 20 mm length and 2 mm width, separated by 13 mm gap, were deposited. A

custom-made stencil shadow mask was used to produced the above pattern with the help of a DC sputtering (Metallifier sputter, Precision Atomics) machine. The DC power, working pressure, and Ar flow rate used were 100 W, 3.5×10^{-3} mbar and 31 sccm, respectively. The resulting electrodes had average thicknesses ranging 105-115 nm.

Gold (Au) contacts were also deposited on the corners of a small glass substrate (8×8 mm), with above same conditions, for Hall effect measurements.

2.3 Characterisation techniques

As-deposited and annealed thin films (at 150 ºC and 300 ºC) under different annealing times (1 h, 12 h, and 24 h) were characterised by the following techniques. It is important to mention that the annealing period was varied only for annealing temperatures of 300 ºC, once the best thermoelectric results were achieved for this temperature. Due to time constraints, it was not possible to study the influence of higher annealing temperatures. The annealing process was carried out on a hot plate under ambient air.

The thickness of ISO films on silicon substrate was determined using a surface profilometer (Dektak 6M, Veeco).

Structural characterisation was realized by X-ray diffraction (XRD) using a PANalytical X´Pert PRO with Cu Kα radiation (λ = 1.540598) from 15º to 65º. In order to analyse only the ISO characteristic peaks, an offset was made to silicon substrate peak. Surface roughness was inspected by atomic force microscopy (AFM) using Asylum MFP-3D system in non-contact mode on an area of $2 \times 2 \mu m^2$, and determined using an analysis software, Gwyddion [44]. The surface morphology and atomic concentration were examined by scanning electron microscopy (SEM) using a Zeiss Auriga and energy-dispersive X-ray spectroscopy (EDS), respectively. SEM was operated at 2 kV, with an aperture size of 30 μm and a working distance of 5.2 nm.

The optical properties, namely the optical transmittance (T%) and optical absorbance were measured in the wavelength range from 190 to 1100 nm using a UV/Vis spectrophotometer UV4 from Unicam. A blank quartz glass was used as reference.

Electrical resistivity, ρ, was measured at room temperature by the four-point probe method (FPP) using a semiconductor parameter analyser (Keithley 4200-SCS) attached to the Sigmatome 1160 series probe station. Additionally, Hall mobility, μ_H, and carrier concentration, n, were evaluated at room temperature by Hall effect measurements using the van der Pauw configuration at constant magnetic field of 0.2 T (MMR H5000).

The Seebeck coefficient was measured in air at room temperature using a custom-made set-up, built by the HGL group, consisting in a 2-point geometry as illustrated in figure 2.1. According to what was mentioned in Chapter 1, the Seebeck coefficient is measured with respect to two materials. If a reference material is used, then the Seebeck coefficient of a specific material can be determined [10]. In this dissertation, copper pins were used in the measurement of the developed potential. Therefore, copper was used as the reference material.

The slope method was used, in which the temperature supplied by one Peltier module (Peltier heater) is varied while keeping the other module at a constant temperature (Peltier cooler). This temperature gradient was achieved by using a sourcemeter (Keithley 2604B)

connected to each Peltier module by different channels. Since the relation between V and ΔT is linear for small temperature differences, a maximum ΔT no more than 3 K was preferred for the Seebeck coefficient extraction.

A quasi-steady-state technique was chosed, in which the temperature difference was varied slowly as the measurements were conducted in a continuous way. Both temperature difference and voltage were measured simultaneously using K-type thermocouples connected to a temperature reader (Omega HH501BJK) and a nanovoltemeter (Keithley 2182A), respectively [10].

The two thermocouples were ajusted near the Mo electrodes and covered with a non-conductive thermal paste, in order to enssure a good thermal contact. After the acquisition of several points, the slope of the developed potential as a function of temperature difference was used to determine the Seebeck coefficient value [10].

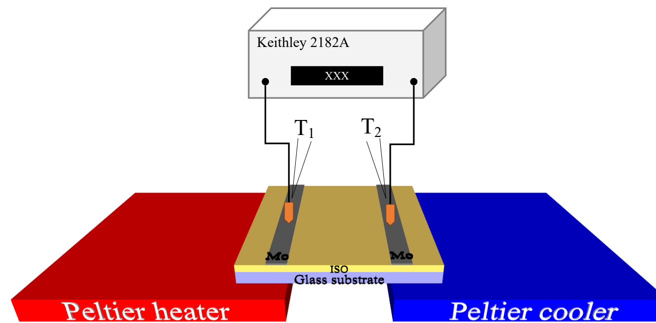

Figure 2.1: Demonstration of the 2-point geometry used for thermoelectric measurements of ISO thin films. Two copper pins at a distance of 12 mm of each other on top of Mo electrodes are used for acquisition of thermoelectric voltage. The two K-type thermocouples are placed a few mm from the copper pins for temperature readings.

Chapter 3

Results and Discussion

This chapter comprises all the characterisation results obtained for sputtered ISO thin films with different configurations, such as $\%O_2$, annealing temperature, and annealing time. The performed characterisation covers the study of different properties of the films namely structural, morphological, compositional, optical, electrical, and thermoelectric. This analysis is intended to help on the evaluation of these parameter's influence on the properties of ISO thin films, especially on thermoelectric properties.

3.1 Sputtering atmosphere influence on the growth rate

Sputtering is a well-known and very used technique for thin films deposition. Usually an inert atmosphere, typically composed of argon (Ar), is ionised and used to eject atoms from the target to form thin films. The deposition of oxide materials, such as TCOs and TSOs is normaly performed under a reactive atmosphere, namely a mixture of oxygen (O_2) and Ar. As a result, the deposition technique is designated by reactive sputtering and has the advantage of producing more transparent and nearly stoichiometric thin films [45]. ISO is an oxide material and therefore reactive sputtering was the preferred method.

Sputtering parameters can lead to different deposition rates and consequently to different properties on the thin films. In this work, it was studied the influence of oxygen content in the gas mixture on ISO thin films properties. However, in order to analyse this influence it is important to understand how can different gas compositions affect the growth rate of thin films.

As described earlier in Chapter 2, ISO thin films were deposited on different substrates, depending on the characterisation method, at room temperature and under variable $\%O_2$. Oxygen gas content of 3 % and 17 % were studied, in order to analyse the impact of low and high gas content on ISO properties, respectively. In addition, the influence of an inert atmosphere was also studied. All the other sputtering parameters such as target composition, power, working pressure, deposition time, and target-to-substrate distance remained constant.

The as-deposited thin films have a ranging thickness of 198-334 nm. The different thicknesses result from the different growth rates, as it will be shown next, due to various oxygen contents present in the sputtering atmosphere since the deposition period remained constant. Higher thicknesses of 334 nm were obtained under inert atmospheres, while thicknesses of 198 nm and 217 nm were obtained under 3 % and 17 % of O_2, respectively.

Figure 3.1 shows the growth rate of the films as a function of the oxygen content on the total gas mixture. As observed, the growth rate is dropped from $11.13\,\mathrm{nm\,min^{-1}}$ to

7.24 nm min^{-1} as %O_2 is increased. However, at %O_2 = 3% the growth rate achieves its minimum at 6.60 nm min^{-1}.

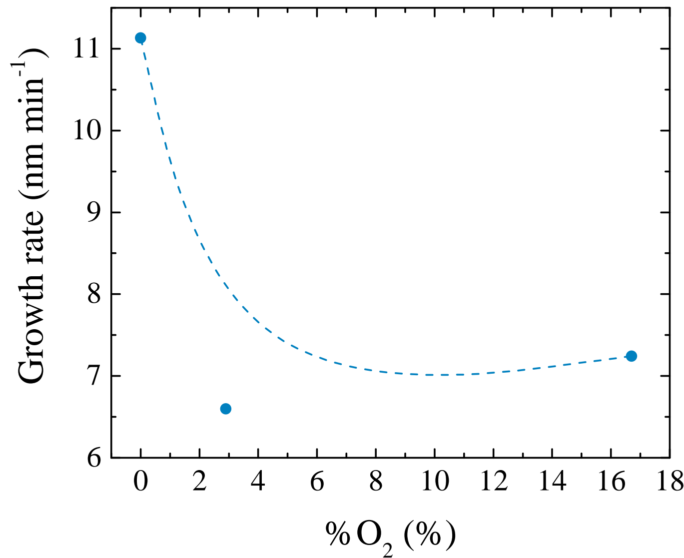

Figure 3.1: Dependence of the growth rate on %O_2 present in the sputtering atmosphere.

Several factors can be pointed out to justify this decrease. In order to eject the target material, the incident ions should have enough energy to dissociate the bond between the target atoms. For instance, the bond dissociation energy for Si-O is 799 kJ mol^{-1} whereas for In-O is 346 kJ mol^{-1} [46]. In turn, the energy to sputter a metal atom is lower than for a metal-oxide molecule.

The reduction of Ar ions as the %O_2 increases can also be one of the reasons, leading to lower growth rates since oxygen ions are lighter than argon ions and therefore the momentum transfer to target is reduced.

In addition, the target surface starts to get oxidised at high %O_2. Since the sputtering yield is lower for the compound formed at the target surface, the growth rate decreases with target contamination [47]. However, this phenomenon can be observed to a great extent for metal targets rather than for ceramic targets. Nevertheless, this effect is diminished when using only Ar atmosphere once this gas is inert.

Re-sputtering of the film by energetic oxygen anions produced in the plasma and accelerated to the substrate is another phenomenon that can occur. Finally, sputtered particles may reduce their kinetic energy due to scattering caused by collisions with the ionised gas plasma, which can suffer a variation in the composition during the deposition time. Therefore a lower mean free path has negattive effect on growth rate [48].

These are some of the phenomena observed for reactive sputtering that can be on the basis of the growth rate reduction. Similar results were obtained for ITO films deposited either by RF-sputtering or DC sputtering [4, 49–51], and for DC sputtered IZO films [52].

3.2 Characterisation of ISO thin-films

3.2.1 Structural characterisation

The structure of thin films can effect other characteristics, namely electrical properties. Hence, structural characterisation is one of the most performed studies to understand the phase structure of thin films.

The characterisation was realised to ISO thin films deposited at room temperature on Si substrate and decoupling of the silicon substrate was performed to reduce its peak.

Figure 3.2 presents the diffractograms for different post-annealed thin films prepared with different $\%O_2$ in the sputtering atmosphere.

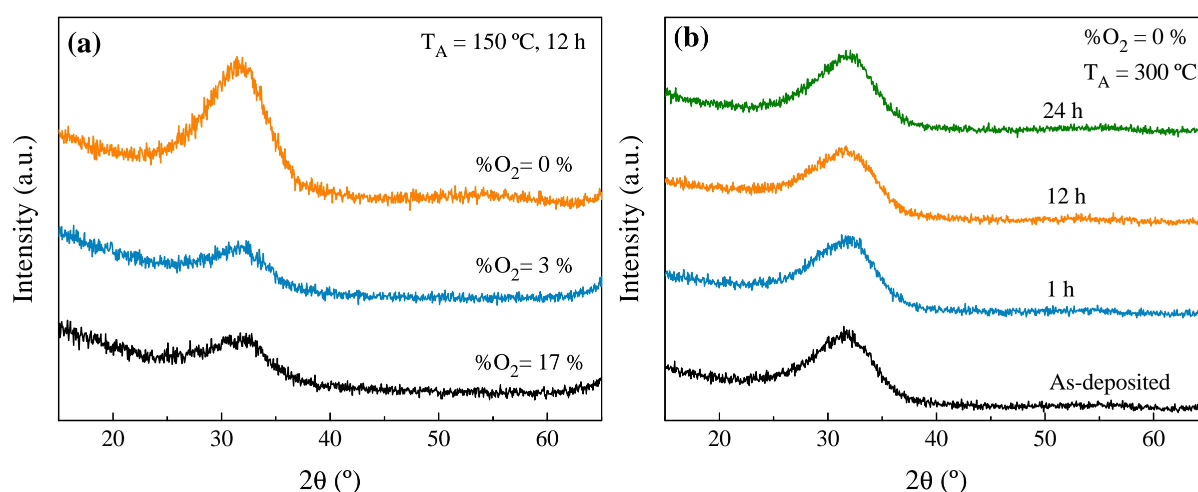

Figure 3.2: Structure of ISO thin films for (a) different $\%O_2$ annealed at 150 ºC for 12 h and (b) for different annealing periods at 300 ºC.

In figure 3.2(a) and (b), it is discernible an enhanced broad peak for thin films deposited under an atmosphere with $\%O_2$ = 0%. This can lead to the conclusion that the films are not completely amorphous, presenting a nanocrystalline-like structure. If some nanocrystallites are present, then they crystallise in the (222) plane of cubic bixbyite In_2O_3. The diffractograms of the remaining two series of films, prepared with $\%O_2$ of 3 % and 17 %, revealed an amorphous structure and no difference is found between the films. One of the reasons for the difference found between the films may be attributed to different thicknesses, which for films deposited under inert atmosphere is considerably higher.

According to Park *et al.*, the amorphous phase is a mixed state of In and Si atoms [42]. The broad peak position is located at 31.7º and 32.1º for thin films deposited under inert atmoshere and under reactive gas mixture, respectiely, which is higher than the peak position of (222) plane at around 30º found for polycrystalline In_2O_3 [42]. This shift was caused by Si atoms, which possess smaller size (ionic radius=0.40Å) than In atoms (ionic radius=0.94Å). Once Si^{4+} ions substitute for In^{3+} sites in ISO films, the average lattice parameter is shrinked and the broad peak position is increased to the right [42, 53, 54]. On the contrary, for ITO thin films deposited by RF sputtering, the lattice parameter is expanded due to a growth induced

stress [55].

When the films are submitted to thermal annealing, no structural change is observed for all post-deposition conditions once the curves are similar to the as-deposited curve, as depicted in figure 3.2(b) and in figure B.1 (Appendix B). Therefore, annealing at different temperatures and at different periods had no effect on the structure and the various films remained with the same structure as respective as-deposited thin films, once no change was observed in the intensity and width of the broad peak. Consequently, annealing at 300 ºC is not sufficient for a transition from amorphous/nanocrystalline to a more crystalline structure on ISO films. A similar conclusion was reached by Mitoma *et al.* who also studied sputtered ISO films produced from a target with the same composition (90 wt.% In_2O_3:10 wt.% SiO_2): annealing at 600 ºC did not produce any cristallyne structure, so the crystallisation temperature increased with increasing SiO_2 content [39]. The transition to a more crystalline structure is prevented by the substitution of In atoms by Si atoms [6].

The stability observed in the diffractograms when the films are submitted to different annealing temperatures and times resembles to what is found in IZO thin films, where In atoms are replaced by Zn atoms [56]. Moreover, the disposition of In ions in both a-In_2O_3 and a-IZO films is similar to what is found in bixbyite In_2O_3 crystal. The phase separation of ZnO from In_2O_3, requires the rejection of Zn from the c-In_2O_3 structure. However, the kinetics of phase separation is slow and Zn has the effect of stabilizing the amorphous phase. Similar happens to ISO due to the large kinetic barrier required for recrystallisation and the tendency of SiO_2 to preserve tetrahedral coordination [42].

Reports have demonstrated that ISO thin films become amorphous at smaller Si content of 2.8 at.% [42]. In addition, introducing Si atoms in In_2O_3 structure keeps short and long range order of bixbyite structure. When a certain concentration of Si atoms is surpassed the long range is broken, so the short range is preserved and the oxide semiconductor is amorphous. The simple fact that smaller concentrations of Si atoms induce an amorphous phase is due to strong bonding energy of Si-O bonds, so tetrahedral bonding is easily accommodated in the short range order than into long range because of rigidity of cristalline In_2O_3 matrix [42].

Increasing %O_2 yields weaker broad peaks. According to what was said previously, the dissolution of Si atoms in the In_2O_3 matrix results in amorphous phase. Moreover, crystallisation temperature increases with SiO_2 content. As a consequence, it is expected that films with %O_2 = 0% possess lower SiO_2 content, resulting in a strengthened broad peak as opposed to %O_2 = 3% and %O_2 = 17%.

In order to estimate possible crystallite sizes, the Debye-Scherrer equation was applied to the peak [57]:

$$D = \frac{0.9\lambda}{B\cos\theta} \tag{3.1}$$

where λ is the X-ray wavelength (1.54 Å), θ is the Bragg diffraction angle, and B is the full width at half maximum (FWHM).

The possible crystallite sizes ranged between 1.00 and 1.70 nm, which can help to define the structures as amorphous or nanocrystallines depending on the %O_2 present in the deposition atmosphere. Bigger crystallites (1.70 nm) were obtained for films deposited with 0

% of oxygen, whereas as the $\%O_2$ increased, smaller sizes were obtained with 1.13 nm and 1.20 nm for $\%O_2$ = 3% and $\%O_2$ = 17%, respectively. These results are in agreement with the obtained diffractograms since crystallites with bigger sizes usually represent a less amorphous structure [4, 58]. With increasing annealing temperature and time, the crystallite sizes decreased 0.10 nm for all set of films, due to possible effective substitution of In^{3+} sites by Si^{4+} ions [43].

3.2.2 Morphological characterisation

Surface morphology was investigated by SEM. In figue 3.3 a difference in the morphology is observed for films deposited with different $\%O_2$ in the sputtering atmosphere. As discussed in the previous section, possible nanocrystallite inclusions can be present in the amorphous structure, mainly for films deposited under inert atmospheres which can therefore be regarded as nanocrystalline, with sizes that change very slightly with post-deposition conditions. Since no significant difference was observed after thermal treatment of as-deposited thin films (figure C.1 in Appendix C), SEM images obtained after annealing at 300 ºC for 24 h are discussed for comparison purposes.

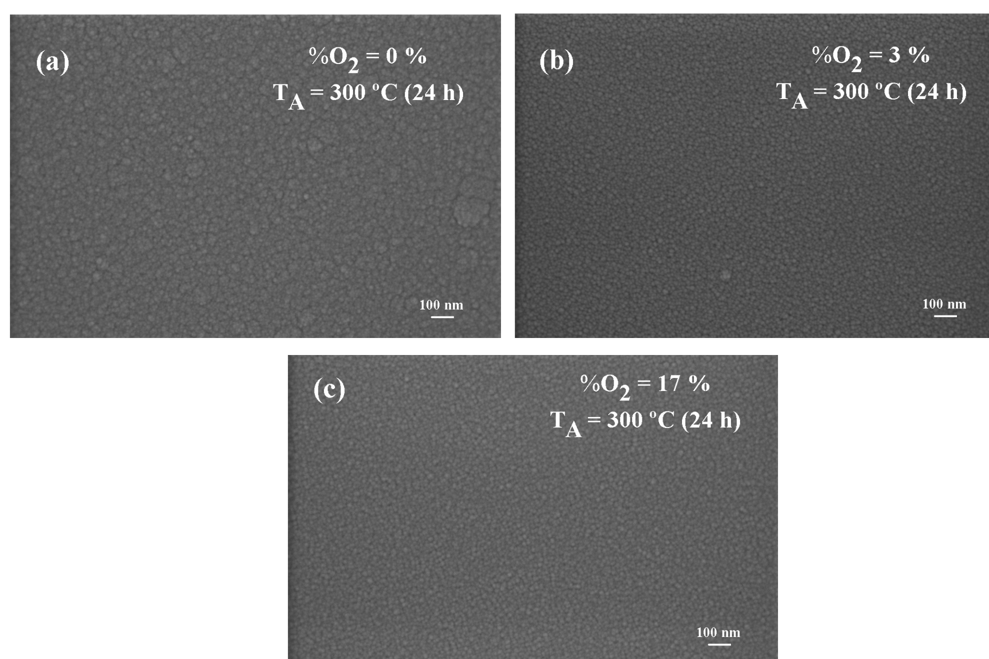

Figure 3.3: SEM images of films deposited under different oxygen contents and annealed at 300 ºC for 24 h: (a) 0 %, (b) 3 %, and (c) 17 %.

SEM images reveal smooth surfaces with no defects such as cracks, protrusions, and pinholes. Smaller feature sizes are visible for films deposited under inert atmosphere, although for films deposited under atmospheres with $\%O_2$ of 3 % and 17 % the features are very small. These observations agree with the previous XRD analysis, in which the last two set of films demonstrated to be amorphous. Furthermore, the roughness seems to decrease with

%O_2. Different thicknesses obtained for each set of thin films can help to explain the variations observed for the surface morphology.

Amorphous and nanocrystalline ISO thin films with similar morphology were also obtained by other authors who studied ISO thin films [42, 43, 59]. When comparing with other InOx-based amorphous materials deposited at different %O_2, surface morphology is very similar [4, 60].

The surface morphology was also confirmed by AFM on an area of 2×2 μm, as depicted in figure 3.4. As similar to SEM images, thin films deposited under inert atmosphere present higher feature sizes, whereas the morphology of films deposited under different %O_2 remains very similar with features evenly distributed on the surface. The small observed features are related with Si content, which may be different depending on the deposition conditions as discussed in the previous section, and to insufficient deposition temperature which did not allow enough energy for nucleation (crystallisation temperature increases with silicon content).

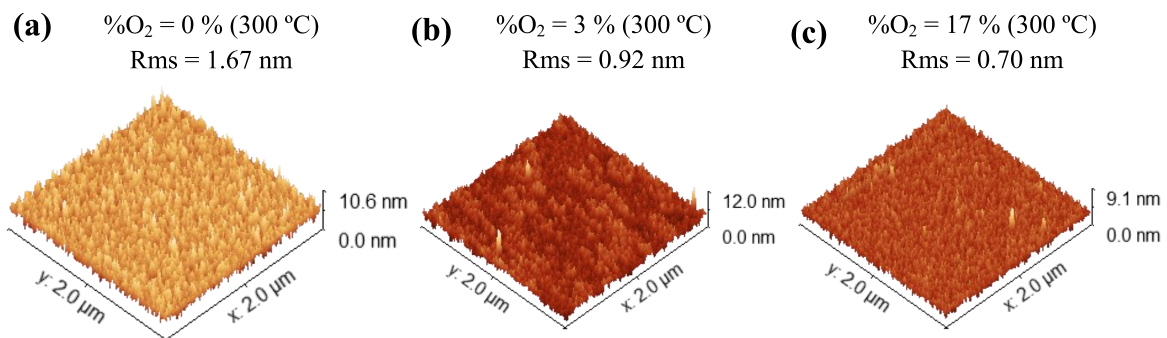

Figure 3.4: AFM images of thin films sputtered at different oxygen contents and annealed at 300 ºC for 24 h.

Root-mean-square roughness (r_{RMS}) was determined using a data analysis software (Gwydion). The obtained values can be found in table 3.1. By analysing the roughness values, it can be concluded that different behaviours are found to be dependent on the %O_2 used during sputtering. For films deposited under argon atmosphere, the feature sizes are bigger for as-deposited films resulting in higher roughness. As the annealing process is conducted, the size is decreased, leading to even small features for annealing temperatures of 300 ºC, and consequently to a lower roughness. For this last annealing temperature, annealing times up to 12 h resulted in constant roughness, whereas when annealing for 24 h the roughness was increased in 65 %.

The same is not visible as %O_2 increases. By analysing first the films deposited under %O_2 = 3%, roughness is decreased after annealing at 150 ºC. Nevertheless, annealing at higher temperatures leads to an increased roughness, where annealing times of 1 h and 24 h presented the higher roughness values for these films.

The opposite is found for films sputtered at high %O_2. Annealing has the same effect on roughness decreasing, but high annealing at 300 ºC for the same period lead to an increased roughness when compared to annealing at 150 ºC. The effect of annealing time on these films is

different from the last two group of films. In this case, roughness increases only when annealing for 12 h, while it decreases for annealing times of 1 h and 24 h. Nonetheless, annealing at 300 ºC resulted in an increased roughness for films deposited under reactive atmospheres, as opposite to annealing at 150 ºC.

In general terms, films are smoother when sputtered under mixing atmospheres of Ar and O_2. Likewise, Mitoma *et al.* achieved lower (r_{RMS}) of 0.23 nm when depositing only 10 nm of a-ISO thin films [39]. Additional AFM images of as-deposited thin films are depicted in figure C.2 for comparison.

Table 3.1: Roughness variation for thin films annealed at different temperatures and times.

%O$_2$ (%)	**Roughness (nm)**				
	As-deposited	**150 ºC (12 h)**	**300 ºC (1 h)**	**300 ºC (12 h)**	**300 ºC (24 h)**
0	1.82	1.27	1.01	1.01	1.67
3	0.86	0.73	0.89	0.75	0.92
17	1.01	0.79	0.75	0.86	0.70

3.2.3 Compositional analysis

In order to study the effect of growth rate on the composition of the thin films, EDS analysis was carried out. As it can be seen in figure 3.5, incorporating oxygen in the sputtering atmosphere leads, in turn, to similar contents of oxygen (O), silicon (Si), and indium (In). However, Si and O are the elements with more at.% in these films. On the contrary, an inert atmosphere conducts to lower contents of Si when compared to other films, while O and In are the elements with more at.%.

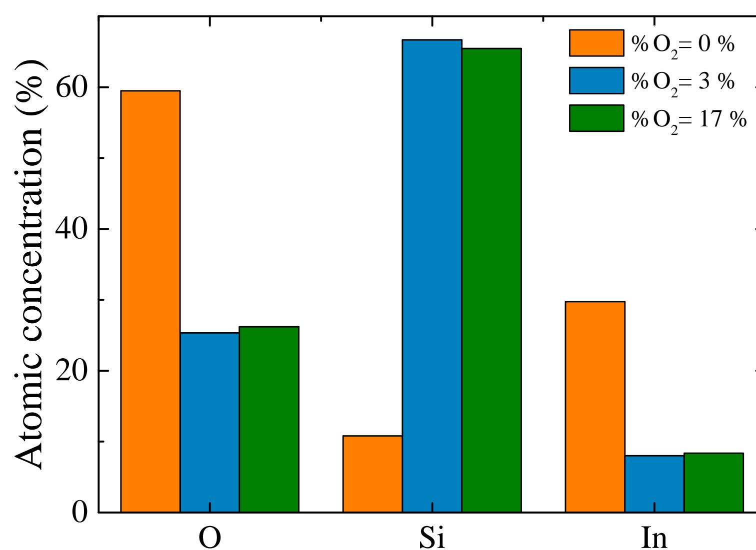

Figure 3.5: Atomic concentration of silicon and indium for as-deposited ISO thin films.

This effect is related with the bond dissociation energy which is bigger for Si-O than In-O, being 799 kJ mol^{-1} and 346 kJ mol^{-1}, respectively [46]. As a consequence, Ar ions (Ar^+) may

not have enough energy to break the bond between Si and O elements resulting in films with only 10.8 at.% of Si. Hence, In and O are the preferred sputtered elements.

As oxygen is added during deposition, oxygen atoms are converted into oxygen ions (O^{2-}) that are more energetic than Ar^{+} ions. Therefore, oxygen anions possess enough energy to sputter Si atoms yielding similar values of 66.7 at % and 65.4 at % for 3 % and 17 %, respectively. Re-sputtering of the films by O^{2-} ions can be one of the reasons for low concentration of In and O elements in these two set of films.

This discrepancy justify the fact that films deposited with $\%O_2$ = 0% are less amorphous and can be defined as nanocrystaline since lower concentration of Si atoms interfere with the structure, allowing the appearing of nanocrystallites. In constrast, in films prepared under 3 % and 17 % of oxygen more SiO_2 may be present, resulting in smoother surfaces.

3.2.4 Optical characterisation

Investigation of optical properties of oxide materials can help to relate band structure with other properties.

Transmittance measurements (190-1100 nm) were carried out to ISO thin films deposited on quartz glass and are presented in figure 3.6. The transmittance of each set of thin films, for different annealing temperatures and periods has no meaningful variation, with exception for films deposited under an inert atmosphere, and therefore the curves for annealing temperature of 150 ºC (12 h) are presented for comparison purposes (figure 3.6(a)).

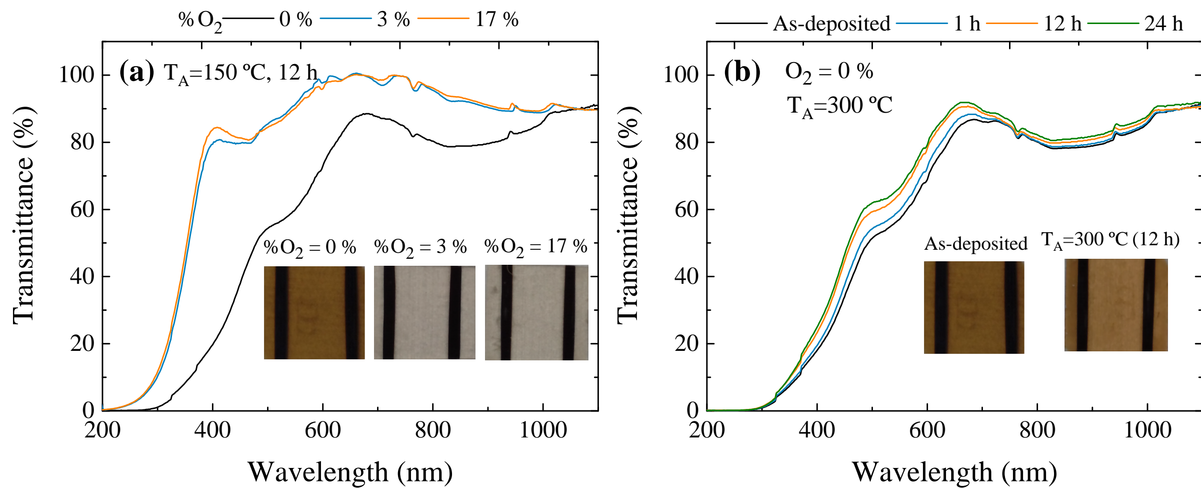

Figure 3.6: Transmittance of ISO thin films deposited under sputtering atmospheres with different $\%O_2$ and annealed a) at 150 ºC and b) at 300 ºC for different periods.

Films deposited under a reactive atmosphere are more transparent than films deposited under an atmosphere with only Ar, and the latter presents a dark yellow colour. For instance, at 550 nm the optical transmittance is 60 %, which is lower than reported values [6, 43]. On the contrary, thin films deposited under reactive atmospheres possess high optical transmittance and no significant difference is noticeable when using different $\%O_2$ (figure 3.6(a)). Films

deposited under 3 % and 17 % of oxygen possess 91.3 % and 90.1 % of transmittance at 550 nm, respectively.

When the films are submitted to different annealing periods, only the darker thin films evidence a small enhancement in the transmittance for 12 h and 24 h, as observed in the inset of figure 3.6(b). This enhancement can be due to possible oxygen vacancies annihilation from residual oxygen present in the film or on the top surface. The colour is then converted from dark yellow to a lighter yellow. The more transparent films have not suffered the same improvement, as observed in figure D.1 (appendix D), where all the curves for as-deposited and annealed at different periods have the same transmittance values.

In Appendix D is also shown the absorbance curves (figure D.2) for different annealing periods. Once again, there is no difference between the curves for the more transparent films, but the same does not occur for the darker films. Notwithstanding, all the thin films absorb radiation in the ultraviolet region.

In the ultraviolet region (<400 nm), the transmittance is decreased for the different set of films due to transitions inside the band. As a result, optical bandgap, E_{opt}, can be determined by Tauc's relation [53], assuming a parabolic energy band structure for the conduction band:

$$\alpha hv = A(hv - E_{opt})^n \tag{3.2}$$

where α is the absorption coefficient, hv is the photon energy, A is a proportionality constant, and n is a coefficient dependent on the transition.

The relation between the absorption coefficient and the absorbance is given by

$$\alpha = \frac{2.303A}{t} \tag{3.3}$$

where t is the thickness of the thin film, and A is the absorbance.

Tauc's plot is obtained by plotting the absorption coefficient, $\alpha^{\frac{1}{n}}$, with respect to photon energy, hv, being the latter determined as follows:

$$hv = \frac{1240}{\lambda} \tag{3.4}$$

where λ is in nm. The power factor, n, has different values depending on which transition is being evaluated. In this case, ISO is a material with allowed direct transition, resulting in $n = \frac{1}{2}$ [51, 53]. The photon energy, in eV, in which absorption coefficient is zero gives the energy bandgap.

Figure 3.7 illustrates the Tauc's plot for different annealing conditions. The bandgap tends to increase with $\%O_2$, as observed in figure 3.7(a), resulted from an increase on energy levels for optical absorption. The decrease on the growth rate, which leads to a more Si content, and the fact that higher $\%O_2$ fills absorptive defect states caused by oxygen deficiency can be on the basis for energy level increase [61]. Crystallisation can also have an impact on the bandgap increase, as observed by Mitoma *et al.*, in which the optical bandgap increased when ISO changed from amorphous to polycrystalline structure [53]. In this work, the studied annealing temperatures were not sufficient to undergo a crystallisation to that extent, as all the diffractograms remained similar with annealing. Even if some crystallisation starts to happen

with annealing for films deposited with no oxygen, although not visible in the diffractograms, the influence on the bandgap is very small. Furthermore, a reduction on E_{opt} from 3.07 eV to 2.82 eV was observed when Si content increased, namely when ISO changed to amorphous, as reported in ref. [42]. This conclusion can not be applied in this case since it was observed an increase on E_{opt} with $\%O_2$, which resulted in more Si content in the films and therefore a more pronounced amorphous structure. Moreover, the reported values are below of those calculated in this work.

When the films are submitted to thermal treatment, different cases are found. First, E_{opt} suffers a very small increase for 0% of O_2. The increase in E_{opt} can also be due to an increase in charge carrier concentration since the lowest states in the conduction band are blocked and absorption can only occur for higher energy states. However, when $\%O_2$ increases, E_{opt} increases as well for annealing temperatures of 300 ºC and for annealing periods of 1 h and 12 h. A decrease is observed for 24 h as annealing period. The oscillations in the optical bandgap can be a consequence of charge carrier concentration variation.

From this bandgap determination, it is concluded that thin films prepared with 0% O_2 are more stable since their E_{opt} does not vary in a high extent. Table 3.2 resumes the determined E_{opt}.

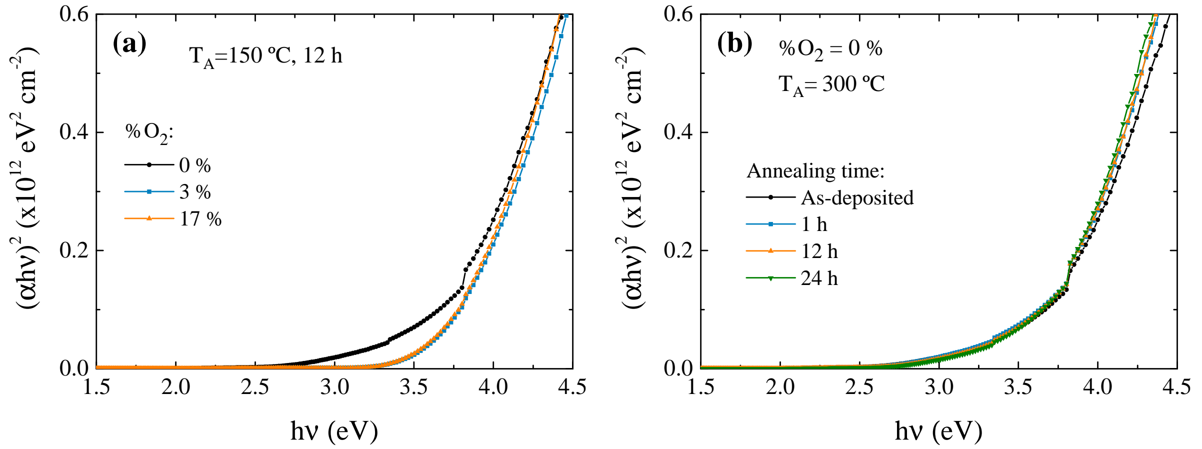

Figure 3.7: Optical bandgap determined by Tauc plot for (a) films annealed at 150 ºC for 12 h, and for (b) films deposited under inert atmosphere and annealed at 300 ºC for different periods. The curve for as-deposited thin films is given for reference.

Table 3.2: Optical bandgap for ISO thin films annealed at different conditions.

$\%O_2$	Eg (eV)				
	As-deposited	**150 ºC (12 h)**	**300 ºC (1 h)**	**300 ºC (12 h)**	**300 ºC (24 h)**
0	3.71	3.73	3.73	3.74	3.75
3	4.03	3.79	3.81	3.85	3.83
17	4.11	3.82	3.83	3.87	3.83

3.2.5 Electrical characterisation

The study of the electrical properties of ISO thin films is presented below and covers the relation between resistivity and electrical parameters obtained by Hall effect measurements, namely carrier concentration, n, and mobility, μ.

Electrical resistivity, ρ, of ISO thin films on glass substrates was first measured using four-point probe method (FPP). The effect of post-deposition conditions on resistivity is shown in figure 3.8.

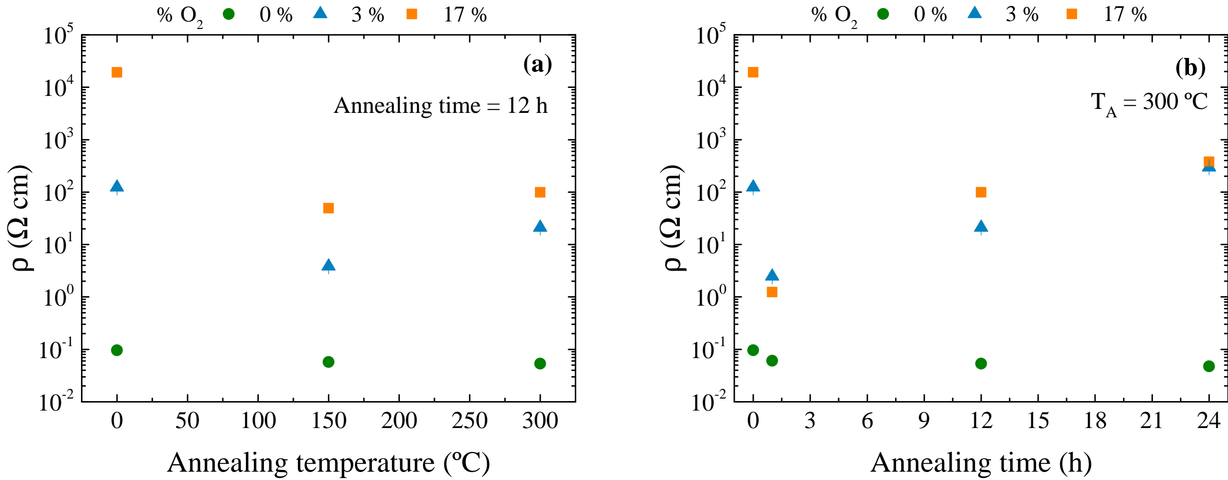

Figure 3.8: Electrical resistivity for (a) different annealing temperatures and (b) different periods (at 300 °C) of ISO thin films deposited under different O_2 content in the sputtering atmosphere.

In oxide materials it is well reported that one of the main contributors to electrical conductivity is the presence of oxygen vacancies, V_O. In InO_x-based materials, the charge is transferred from the indium to oxygen atoms due to strong ionicity of these oxides. The conduction band is then formed by unoccupied indium 5*s* orbitals, whereas the valence band is constituted by fully occupied 2*p* orbitals.

At room temperature, oxygen vacancies are ionised and each vacancy contributes with two free electrons [4]. Oxygen vacancies, formed by In atoms with dangling bonds, act as shallow donors with energy levels near the conduction band edge. Hence, In atoms with V_O are considered conductors while fully oxidised In atoms are considered as insulators (figure 3.9).

When Si atoms are added to indium oxide structure, the formation of V_O is suppressed since the bond dissociation energy is much higher than In-O [39, 41, 62].

The deposition parameter studied in this work, $\%O_2$, has an important contribution to the formation, or not, of oxygen vacancies. In figure 3.8, it is shown that resistivity is considerably higher for thin films deposited under reactive atmospheres.

During deposition, some oxygen atoms can be incorporated in the thin films filling the oxygen vacancies created during sputtering [40]. In addition, EDS confirmed higher content of Si in films produced under higher $\%O_2$, which in turn require a small amount of oxygen to occupy the oxygen-deficient sites [39]. Moreover, structural defects induced by energetic oxygen ions bombardment, low growth rates, and low In content found in the films can help

to explain the higher values for resistivity [6, 48, 63]. Therefore, the films with the lowest resistivity are found for %O_2 = 0%.

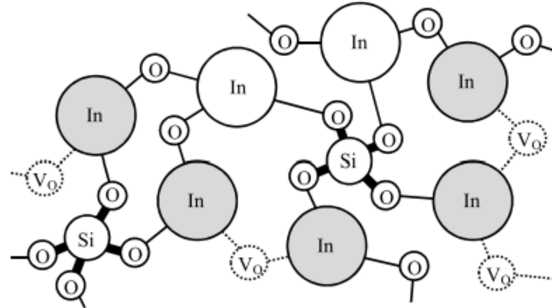

Figure 3.9: Illustration of ISO thin films constitution, where the grey circles are conductors and the white circles are insulators. The incorporation of Si supress the formation of oxygen vacancies (V_O). From [39]

With annealing at 150 ºC, resistivity is decreased, although in a lower degree for films prepared under %O_2 = 0%. However, when annealing at 300 ºC the resistivity slightly increases for the two set of films with higher %O_2. Nevertheless, thin films fabricated at 3 % of O_2 have lower resistivity than films deposited under 17 % of O_2. With respect to films fabricated at %O_2 = 0%, the resistivity is again decreased.

For different annealing periods at 300 ºC, the resistivity is diminished for all the thin films at annealing periods of 1 h. However, the resistivity is enhanced for films deposited under 3 % and 17 % of O_2 when the annealing time is increased to 12 h and 24 h, while is decreased for 0 % of O_2.

In parallel, electrical parameters measured by Hall effect can help to justify the observed results. The relation between the three quantities, ρ, n, and μ with post-deposition conditions are represented in figure 3.10. It was not possible to measure these quantities for as-deposited and for annealing temperatures of 150 ºC and 300 ºC (24 h) due to very high resistivities, or low mobilities and carrier concentrations present in films deposited at %O_2 = 3% and %O_2 = 17%.

As seen in figure 3.10, resistivity is always decreased regardless of the annealing temperature and period for films deposited under 0 % O_2. After annealing at 150 ºC, the mobility increases while the carrier concentration is slightly decreased. This can be explained by the fact that adsorption of oxygen can annihilates some of the V_O, reducing the carrier concentration of the films. Moreover, the increase on mobility can be justified by a local distortion in the structure. This distortion could lead to overlap of 5*s* orbitals of In atoms, enhancing the mobility and therefore the conductivity [53]. In addition, since mobility can be affected by impurity scattering centres, such as ionised (V_O and Si^{4+} cations) and neutral impurities (for instance Si atoms), the reduction of n could have led to a decrease of scattering centres that affect the conductivity, leading to higher conductivities [6, 40, 43, 63].

An enhancement on n is observed when annealing at 300 ºC. Although residual oxygen can annihilate oxygen vacancies, it is possible that some V_O remained. Structural rearrangement

with annealing can favour the release of some of the weakly bounded oxygen atoms (V_O formation), contributing with two free electrons to conductivity although this can happen in a lower degree [42, 53]. It is more likely that an effective substitution of In^{3+} by Si^{4+} with annealing leads to an excess electron, which can contribute to charge carrier concentration and consequentely to the resistivity diminution [38, 40, 43]. An increase in n is followed by a decrease in μ due to scattering centres mentioned previously [42, 43].

The effect of annealing period on electrical parameters of films deposited with 0 % O_2 is exhibited in figure 3.10(b), where the values for as-deposited films are given as reference. An exception to the aforementioned explained behaviour between μ and n is found for annealing periods of 1 h, where both n and μ increase with annealing, although n increases very little and may have very low impact on μ.

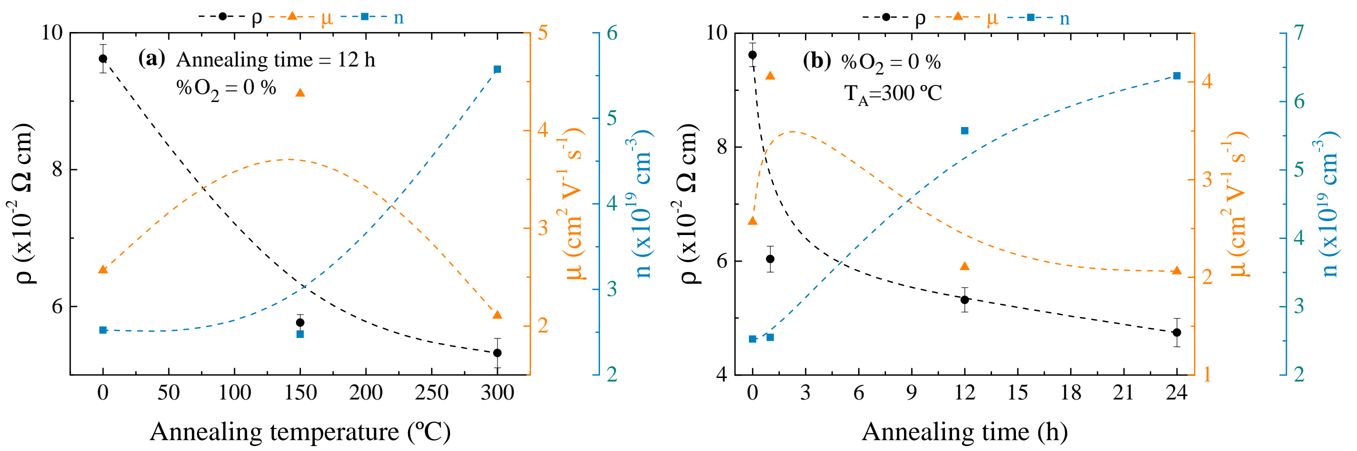

Figure 3.10: Influence of (a) annealing temperature and (b) annealing period on resistivity, mobility, and carrier concentration for thin films deposited under 0 % of O_2.

Table 3.3 represents the obtained measurements for thin films deposited under 3% and 17% of oxygen and annealed at 300 ºC for 1 h and 12 h since the lowest resistivities were achieved for these conditions. As annealing period increases, n decreases for both group of films because oxygen is adsorbed and fills the oxygen vacancies. As a consequence, resistivity is increased. On the other hand, μ increases for 3% O_2 due to a decrease of scattering centres, but the same does not apply for 17% O_2 when the annealing period increases, suggesting that some other situation may be happening. Nevertheless the mobility and carrier concentration values are lower than the values found for films prepared under 0 % O_2.

Table 3.3: Electric characteristics of thin films deposited with 3% and 17% of oxygen and annealed at 300 ºC for different times.

$\%O_2$ (%)		ρ (Ω cm)	μ ($\times 10^{-2}$ cm^2 V^{-1} s^{-1})	n ($\times 10^{19}$ cm^{-3})
3	**1 h**	2.5	4.43	5.74
	12 h	21	5.84	0.51
17	**1 h**	1.24	20	2.52
	12 h	99	0.55	1.16

With regard to annealing periods of 24 h, the annihilation of V_O or the mobility decrease may be the reasons for the resistivity increase. Annealing at 150 ºC, as well as annealing at 300 ºC for 1 h led to possible structural rearrangements with effective substitution of In sites by Si^{4+} and oxygen desorption which are responsible for an enhancement of conductivity, although μ and n values were not possible to be measured at annealing temperatures of 150 ºC.

The electrical properties obtained are lower than the reported by several authors. For instance, the lowest resistivity achieved for films with $\%O_2 = 0\%$ is $4.7 \times 10^{-2}\,\Omega\,cm$, equivalently $21.1\,S\,cm^{-1}$ when annealing for 24 h at 300 ºC, while for films prepared under 3 % and 17 % of O_2 is $2.5\,\Omega\,cm$ and $1.24\,\Omega\,cm$, respectively for annealing at 300 ºC for 1 h. Nevertheless, the same effect of $\%O_2$ on resistivity has also been observed for ISO [41] and for IZO and ITO thin films [64, 65]. The obtained values are high when compared to resistivities of sputtered ISO thin films at room temperature ranging $8 \times 10^{-4}\,\Omega\,cm$ to $1 \times 10^{-3}\,\Omega\,cm$ [6, 43]. Other In_2O_3-based materials such as IZO and IZTO also possess lower resistivities with $5.7 \times 10^{-3}\,\Omega\,cm$ and $9.1 \times 10^{-4}\,\Omega\,cm$, respectively [66, 67].

The variation on mobility and carrier concentration has an impact on resistivity, as previously seen. According to Ioffe's observation, the best carrier concentration for semiconductor thermoelectric materials range between 10^{18}-$10^{20}\,cm^{-3}$. This interval corresponds to degenerate semiconductors or semimetals [26] and it was observed for ISO thin films. Similar values of n found in films deposited under 0 % of oxygen were also obtained by other authors [40, 43]. With respect to mobility, the obtained values (between 2.06 to $4.37\,cm^2\,V^{-1}\,s^{-1}$) are lower than the values found in the literature which can be up to ($\sim 35\,cm^2\,V^{-1}\,s^{-1}$) [43].

3.2.6 Thermoelectric characterisation

In this section the thermoelectric properties, characterised at room temperature, are presented for films prepared under inert atmospheres. The remaining films could not be characterised since their resistance was equal or higher than the impedance of the nanovoltmeter. Before analysing the results, some considerations regarding the method for Seebeck coefficient determination are given.

When extracting the raw data, it is very important to check for hysteresis since it can be an indication of poor thermal or electrical contact, which in turn can lead to erroneous measurements. Figure E.1 (Appendix E) illustrates the used method for extracting the relative Seebeck coefficient. Low hysteresis was confirmed by the similar linear evolution of the raw data: the "up"curve corresponds to measurements as the temperature difference is increased and the "down"corresponds to measurements for decreasing temperature difference.

The Seebeck coefficient of ISO samples was determined by the quasi-static transient method and measured with respect to copper (electrodes). Hence, the absolute Seebeck coefficient for ISO is given according to

$$S_{ISO} = S_{Cu} + S_{reading} \tag{3.5}$$

where S_{Cu} is $3.15\,\mu V\,K^{-1}$, previously measured, and $S_{reading}$ was obtained by the slope of the raw data, according to figure E.1 given as an example in appendix E.

It is necessary to take into account the sign convention. The relative Seebeck coefficient, $S_{reading}$, present in the previous equation is given by the following equation, where $\frac{\Delta V}{\Delta T}$ is the slope of the raw data. Therefore, the absolute Seebeck coefficient determined for ISO thin films is negative, confirming that this oxide is an n-type semiconductor.

$$S_{reading} = -\frac{\Delta V}{\Delta T} \tag{3.6}$$

The following figure illustrates the relation between resistivity and Seebeck coefficient on thin films deposited under inert sputter atmospheres.

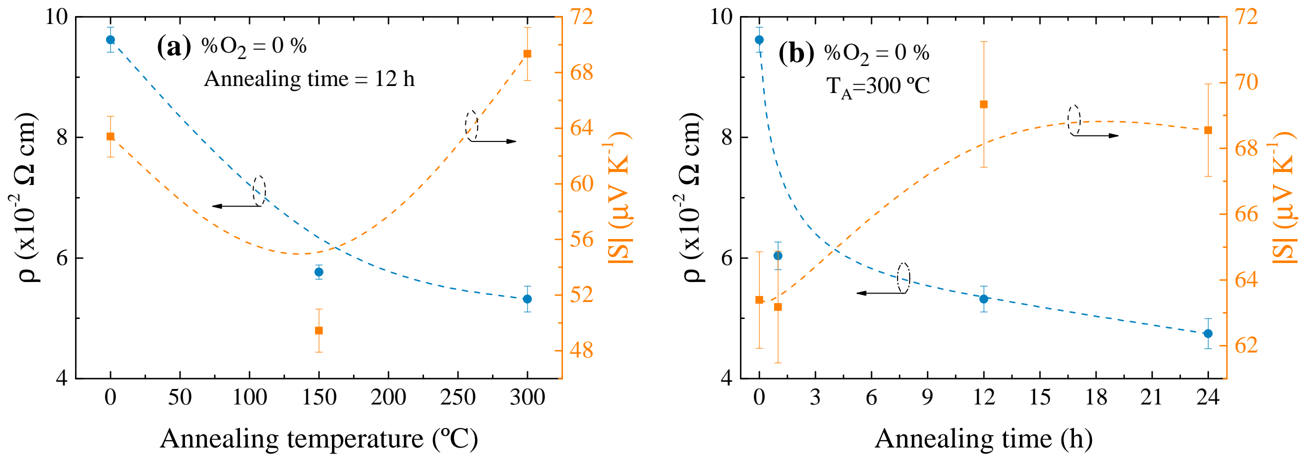

Figure 3.11: Relation between electrical resistivity and Seebeck coefficient for different (a) annealing temperatures and (b) annealing periods of films deposited with 0% O_2. The absolute Seebeck coefficient is given in module.

The relation between conductivity and the Seebeck coefficient is meant to be reciprocal for degenerated semiconductors (high n), meaning that an increase in the conductivity leads to a decrease on the Seebeck coefficient (figure 1.3). By observing the figure 3.11, as the resistivity decreases with annealing temperature (conductivity increases), the Seebeck coefficient, decreases from $-63.4\,\mu\mathrm{V\,K^{-1}}$ to $-49.5\,\mu\mathrm{V\,K^{-1}}$ as expected.

Carrier mobility contributes to electrical conductivity, according to equation 1.2. This parameter is the main contributor for electrical resistivity reduction once the carrier concentration slightly decreases from $2.52\times10^{19}\,\mathrm{cm^{-3}}$ to $2.47\times10^{19}\,\mathrm{cm^{-3}}$ after annealing at 150 ºC.

When annealing at temperatures of 300 ºC, the resistivity is further decreased. However, the Seebeck coefficient increases. Theoretically, based on equation 1.3 this should not happen once an opposite relation between charge carrier concentration and Seebeck coefficient is evidenced. Therefore, an increase in carrier concentration due to mechanisms mentioned in section 3.2.5 would suggest a decrease of Seebeck coefficient. In fact, through the Hall-effect measurement it was confirmed that the carrier concentration was increased as expected, but was followed with a decrease in mobility from $4.38\,\mathrm{cm^2\,V^{-1}\,s^{-1}}$ to $2.11\,\mathrm{cm^2\,V^{-1}\,s^{-1}}$. Nevertheless, this decrease has little effect on conductivity once it is improved by carrier concentration.

Equation 1.3 can also be expressed by the following relation (equation 3.7) for degenerate semiconductors, where n is the carrier concentration, m^* is the charge carrier effective mass, k_B is the Boltzmann constant, h is the Planck's constant, e is the carrier charge, and T is the absolute temperature. In the previous section, it was also mentioned the existence of scattering centres which affect the carrier transport. In this case, the contribution of scattering mechanisms to Seebeck coefficient is also represented in this equation by r, which is the scattering exponent [68].

$$S = \frac{8\pi^2 k_B^2}{3eh^2} m^* T \left(\frac{\pi}{3n}\right)^{2/3} \left(r + \frac{3}{2}\right) \tag{3.7}$$

Several scattering mechanisms can effect the relaxation time (time between colisions) and therefore the carrier mobility. Grain boundaries, lattice vibrations, ionised impurities, and neutral impurities are some of the scattering centres found in oxide semiconductors [65].

Although it is not possible to evaluate the dominant scattering mechanim present in this set of ISO thin films, ionised impurity scattering (from possible remaining oxygen vacancies after annealing and cations) is usually assigned to oxide materials [40, 65]. The scattering exponent is 1.5 for this case [69]. After annealing at 150 ºC, the carrier concentration is slightly decreased which reflected in an enhanced mobility due to possible low scattering centres. As a result, the Seebeck coefficient is decreased in spite of the little n reduction. Nonetheless, at 300 ºC the opposite is observed. Therefore, an increase in the scattering rate can help to explain the improvement of the Seebeck coefficient for annealing at 300 ºC, as explained before.

The relation between carrier mobility and charge carrier effective mass, m^* is given by:

$$\mu = \frac{e\tau}{m^*} \tag{3.8}$$

where e is the electron charge and τ is the relaxation time.

Such a reduction in mobility, determines an increase in the effective mass of the carriers. Therefore, since Seebeck coefficient is proportional to the effective mass, as seen in equation 3.7, such an increase of the first sounds to be valid and reasonable. In fact, the improvement in mobility observed for annealing temperatures of 150 ºC can also be explained by an overlap of 5s orbitals of In atoms, which in turn conducts to a lower effective charge mass [53]. Additionally, the reduction in n leads to less scattering centres, contributing to mobility enhancement. Likewise, the Seebeck coefficient improvement for annealing temperatures of 300 ºC seems to be a contribution of both effective charge mass and scattering centres increase.

Similar conclusions can be drawn by analysing the effect of annealing period on Seebeck coefficient. Annealing periods of 1 h leads to a decrease on the Seebeck coefficient, although in a low extent, mainly due to an improvement on mobility. When annealing for 24 h the Seebeck coefficient is decreased from $-69.3\,\mu\text{V}\,\text{K}^{-1}$ to $-68.6\,\mu\text{V}\,\text{K}^{-1}$ due to the enhancement on n since the mobility is slightly decreased from $2.11\,\text{cm}^2\,\text{V}^{-1}\,\text{s}^{-1}$ to $2.06\,\text{cm}^2\,\text{V}^{-1}\,\text{s}^{-1}$ which leads to the conclusion that mobility has a significant effect on Seebeck coefficient.

For annealing periods of 12 h, in spite of the increase on carrier concentration, the Seebeck coefficient is improved due to scattering, which in turn decreases the relaxation time and

mobility, and consequently improves m^*. Nevertheless, annealing at high temperatures and periods leads to an improved Seebeck coefficient in spite of the enhancement on n, allowing to conclude that scattering mechanisms have a significant effect not only on μ but also on S.

The calculated effective charge masses resulted in approximately $\sim 0.3m_e$, which is similar to effective charge mass of conduction band electrons in ITO [70], although annealing at 300 ºC for 12 h conducted to $\sim 0.5m_e$.

The power factor, *PF*, characterises the thermoelectric performance of a material and is calculated by using the following equation:

$$PF = S^2\sigma \tag{3.9}$$

The resulting values for *PF* are presented in figure 3.12, where a maximum of $9.90\,\mu\mathrm{W\,m^{-1}\,K^{-2}}$ is achieved when annealing at 300 ºC for 24 h. The *PF* did not changed much after annealing at 150 ºC, but resulted in higher values when ISO thin films were annealed at 300 ºC for longer periods. This result indicates that thermoelectric performance is dependent on annealing period for high annealing temperatures as 300 ºC.

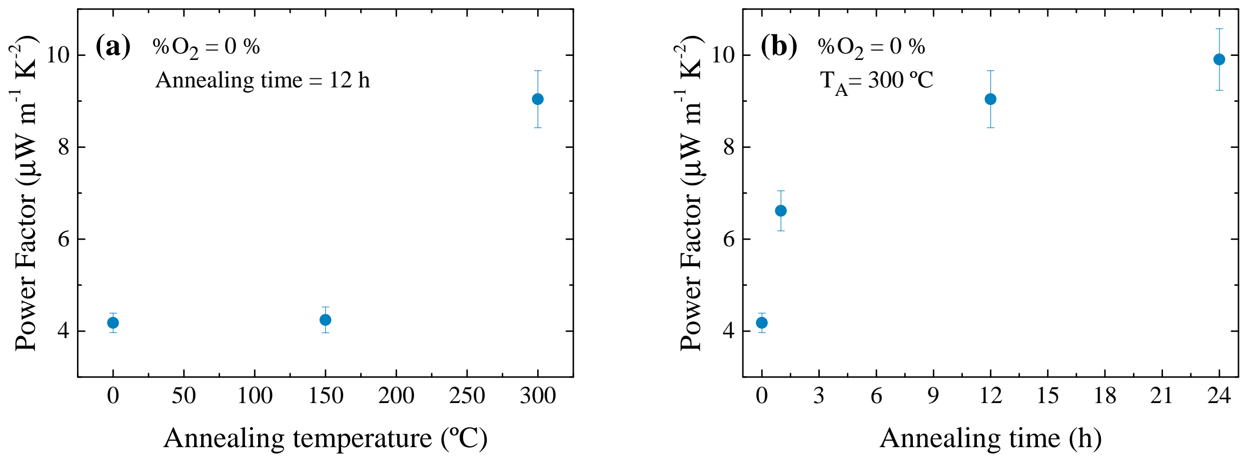

Figure 3.12: Power Factor for (a) different annealing temperatures and (b) different annealing times of films deposited under 0% O_2.

Table 3.4 compares the best thermoelectric properties achieved for ISO thin films prepared under inert sputtering atmospheres with other amorphous oxide materials at room temperature. Although the Seebeck coefficient for ISO is higher than IZO, ITO, and IGZO, the calculated *PF* is lower owing to a higher resistivity.

In order for ISO to be used in real applications, optimisation of deposition and post-deposition conditions is needed.

Table 3.4: Comparison of thermoelectric properties of ISO thin films with other amorphous oxides published in literature.

Oxide	ρ (Ω cm)	n (cm^{-3})	μ (cm^2 V^{-1} s^{-1})	**S** (μV K^{-1})	**PF** (μW m^{-1} K^{-2})	**Ref.**
ISO	4.7×10^{-2}	6.38×10^{19}	2.06	−68.6	10	This work
IZO	5.7×10^{-3}	1.51×10^{20}	7.26	−58	58.90	[67]
ITO	3.4×10^{-4}	$\sim 3.5 \times 10^{20}$	~ 45	~ -30	266.64	[71]
IGZO	5.0×10^{-3}	7.7×10^{19}	-	~ -65	82	[72]

Chapter 4

Conclusions and Future Perspectives

The increasing environmental problems observed nowadays are mainly due to the exaggerated utilization of fossil fuels as consumerism and population increases. As a consequence, more green directives should be implemented to reduce the negative impacts provoked by non-renewable sources of energy.

Heat is one of the most wasted form of energy. Thermoelectric materials can be use in thermoelectric generators to take advantage of this source of energy, since in the presence of a temperature gradient, an electrical potential is generated.

Oxide materials are very studied for applications in TFTs, solar cells, sensors, and as transparent conductors. Materials based on indium oxide are very studied in scientific community for electronic applications, namely transparent electronics.

In this work, properties of Indium Silicon Oxide thin films were studied, namely the thermoelectric properties. For that purpose, thin films were deposited on glass substrate under different sputtering atmospheres (inert and reactive).

The addition of oxygen to the deposition atmosphere led to different growth rates. Although a small oxygen content is usually used to control the film stoichiometry, this addition decreased the growth rate from $11.3\,\mathrm{nm\,min^{-1}}$ to $7.24\,\mathrm{nm\,min^{-1}}$. Several factor are pointed to this reduction, such as the re-sputtering of the thin film by energetic oxygen anions. Moreover, the low mean free path of the sputtered particles towards the substrate is another pointed factor.

The structure of the thin films was also affected by the deposition atmosphere. The thin films revealed to be more amorphous as the oxygen content in the atmosphere, $\%O_2$, increased. For films deposited under an inert atmosphere, some dispersed nanocrystallites can be found embedded in the amorphous matrix since it was observed an increase of the broad peak. These last films can be regarded as nanocrystalline. The substitution of Si^{4+} ions into In^{3+} sites resulted in an amorphous or nanocrystalline phase since the long range order in In_2O_3 structure is broken.

Morphological analysis proved small features for thin films deposited under inert atmospheres. A difference between films deposited at different $\%O_2$ was not perceptible, and annealing did not change the surface morphology, as expected. Consequently, the thin films presented roughness inferior to 1 nm as annealing temperatures and times were used. The compositional analysis confirmed some primary conclusions. Depositions performed under reactive atmospheres led to an increase in Si content in the films, while In is reduced.

Consequently, a variation in transmittance is observed for different deposition configurations. The maximum transparency of 90 % was achieved for films deposited under

reactive atmospheres, while films prepared under inert atmosphere presented a dark yellow colour. The determination of the optical bandgap from absorbance allowed to conclude that ISO is a material with direct transitions between bands. Moreover, the optical bandgap suffered an increase with oxygen content in the sputtering gas due to a reduction of density of states near the conduction band tail. The effect of annealing time led to an increase of optical bangap for films deposited with no oxygen, while films deposited under reactive atmospheres suffered an oscillation on the bangap.

The dissociation bond energy is higher for Si-O than for In-O. As a result, when the films have higher Si content it is more difficult to originate oxygen vacancies (responsible for conduction in amorphous oxide semiconductors). When annealing at 150 ºC for 12 h, conductivity increased due to possible desorption of weakly bond oxygen atoms and to substitution of In^{3+} sites by Si^{4+}.

Hall effect measurements showed an improvement on charge carrier concentration with annealing. The relation between Seebeck coefficient and resistivity, as determined by thermoelectric characterisation, was not reciprocal for certain post-deposition conditions. The enhancement on Seebeck coefficient was attributed to ionised impurity scattering. The maximum power factor was achieved for annealing at 300 ºC and 24 h with a value of $10\,\mu\mathrm{W\,m^{-1}\,K^{-2}}$. However this value remains below to observed for other oxide thermoelectric materials.

Taking into account the observed properties, ISO revealed to be a stable semiconductor, once its properties have suffered very little with post-deposition conditions. This is very important when using this material for electrical and thermoelectric applications since it is expected that the performance does not change much.

In order to improve the performance of ISO as a thermoelectric material, optimisation to thin films fabricated under inert atmospheres is imperial for enhancement of thermoelectric properties. The study of the influence of thickness on electrical properties should also be addressed, as well as the study of different annealing atmospheres and higher temperatures. Moreover, in order to understand the principal scattering mechanism, studies of the influence of electrical properties with temperature should be performed (Hall effect with temperature). XPS should also be performed to confirm the composition and to observe the formation or not of oxygen vacancies. Finally, it would be interesting to perform a micro-Raman spectroscopy and to evaluate the thermal conductivity with different deposition atmospheres and annealing conditions.

Bibliography

[1] IEA. *Renewables Information: Overview 2017*. Tech. rep. 2017.

[2] IEA. *Transforming our World: The 2030 Agenda for Sustainable Development*. 2016. URL: https://sustainabledevelopment.un.org/post2015/transformingourworld.

[3] E. Commision. *Renewable energy - European Commission*. URL: https://ec.europa.eu/energy/en/topics/renewable-energy.

[4] Y. Orikasa, N. Hayashi, and S. Muranaka. "Effects of oxygen gas pressure on structural, electrical, and thermoelectric properties of (ZnO) 3 In 2 O 3 thin films deposited by rf magnetron sputtering." In: *Journal of Applied Physics* 103.11 (2008), p. 113703.

[5] K. Ellmer. "Past achievements and future challenges in the development of optically transparent electrodes." In: *Nature Photonics* 6.12 (2012), pp. 809–817.

[6] H.-M. Lee, S.-B. Kang, K.-B. Chung, and H.-K. Kim. "Transparent and flexible amorphous In-Si-O films for flexible organic solar cells." In: *Applied Physics Letters* 102.2 (2013), p. 021914.

[7] S. Aikawa, N. Mitoma, T. Kizu, T. Nabatame, and K. Tsukagoshi. "Suppression of excess oxygen for environmentally stable amorphous In-Si-O thin-film transistors." In: *Applied Physics Letters* 106.19 (2015), p. 192103.

[8] X. Zheng, C. Liu, Y. Yan, and Q Wang. "A review of thermoelectrics research–Recent developments and potentials for sustainable and renewable energy applications." In: *Renewable and Sustainable Energy Reviews* 32 (2014), pp. 486–503.

[9] D. M. Rowe. *Thermoelectrics handbook : macro to nano*. CRC/Taylor & Francis, 2006.

[10] K. A. Borup, J. de Boor, H. Wang, F. Drymiotis, F. Gascoin, X. Shi, L. Chen, M. I. Fedorov, E. Muller, B. B. Iversen, and G. J. Snyder. "Measuring thermoelectric transport properties of materials." In: *Energy Environ. Sci.* 8 (2 2015), pp. 423–435. DOI: 10.1039/C4EE01320D. URL: http://dx.doi.org/10.1039/C4EE01320D.

[11] Z.-H. Ge, L.-D. Zhao, D. Wu, X. Liu, B.-P. Zhang, J.-F. Li, and J. He. "Low-cost, abundant binary sulfides as promising thermoelectric materials." In: *Materials Today* 19.4 (2016), pp. 227–239.

[12] H. J. Goldsmid. *Introduction to thermoelectricity*. Vol. 121. Springer, 2010.

[13] A. Shakouri. "Recent developments in semiconductor thermoelectric physics and materials." In: *Annual Review of Materials Research* 41 (2011).

[14] M. Cutler and N. F. Mott. "Observation of Anderson localization in an electron gas." In: *Physical Review* 181.3 (1969), p. 1336.

[15] C. Han, Z. Li, and S. Dou. "Recent progress in thermoelectric materials." In: *Chinese science bulletin* 59.18 (2014), pp. 2073–2091.

[16] G. S. Nolas, J. Sharp, and J. Goldsmid. *Thermoelectrics: basic principles and new materials developments*. Vol. 45. Springer Science & Business Media, 2013.

[17] X. Shi, J. Yang, J. R. Salvador, M. Chi, J. Y. Cho, H. Wang, S. Bai, J. Yang, W. Zhang, and L. Chen. "Multiple-filled skutterudites: high thermoelectric figure of merit through separately optimizing electrical and thermal transports." In: *Journal of the American Chemical Society* 133.20 (2011), pp. 7837–7846.

[18] G. Rogl, Z. Aabdin, E. Schafler, J. Horky, D. Setman, M. Zehetbauer, M. Kriegisch, O. Eibl, A. Grytsiv, E. Bauer, et al. "Effect of HPT processing on the structure, thermoelectric and mechanical properties of Sr 0.07 Ba 0.07 Yb 0.07 Co 4 Sb 12." In: *Journal of Alloys and Compounds* 537 (2012), pp. 183–189.

[19] M. Christensen, S. Johnsen, and B. B. Iversen. "Thermoelectric clathrates of type I." In: *Dalton transactions* 39.4 (2010), pp. 978–992.

[20] X. Yan, G. Joshi, W. Liu, Y. Lan, H. Wang, S. Lee, J. Simonson, S. Poon, T. Tritt, G. Chen, et al. "Enhanced thermoelectric figure of merit of p-type half-Heuslers." In: *Nano letters* 11.2 (2010), pp. 556–560.

[21] B. Sothmann, R. Sánchez, A. N. Jordan, and M. Büttiker. "Powerful energy harvester based on resonant-tunneling quantum wells." In: *New Journal of Physics* 15.9 (2013), p. 095021.

[22] L. Hicks and M. S. Dresselhaus. "Effect of quantum-well structures on the thermoelectric figure of merit." In: *Physical Review B* 47.19 (1993), p. 12727.

[23] B. Wang, J. Zhou, R. Yang, and B. Li. "Ballistic thermoelectric transport in structured nanowires." In: *New Journal of Physics* 16.6 (2014), p. 065018.

[24] G. Fiedler and P. Kratzer. "Theoretical prediction of improved figure-of-merit in Si/Ge quantum dot superlattices." In: *New Journal of Physics* 15.12 (2013), p. 125010.

[25] H Beyer, J Nurnus, H Böttner, A Lambrecht, E Wagner, and G Bauer. "High thermoelectric figure of merit ZT in PbTe and Bi 2 Te 3-based superlattices by a reduction of the thermal conductivity." In: *Physica E: Low-dimensional Systems and Nanostructures* 13.2 (2002), pp. 965–968.

[26] A. M. Dehkordi, M. Zebarjadi, J. He, and T. M. Tritt. "Thermoelectric power factor: Enhancement mechanisms and strategies for higher performance thermoelectric materials." In: *Materials Science and Engineering: R: Reports* 97 (2015), pp. 1 –22. ISSN: 0927-796X. DOI: https://doi.org/10.1016/j.mser.2015.08.001. URL: http://www.sciencedirect.com/science/article/pii/S0927796X1500073X.

[27] Y. Liu, Y.-H. Lin, W. Xu, B. Cheng, J. Lan, D. Chen, H. Zhu, and C.-W. Nan. "High-Temperature Transport Property of In2- xCexO3 (0 x 0.10) Fine Grained Ceramics." In: *Journal of the American Ceramic Society* 95.8 (2012), pp. 2568–2572.

[28] G. Ren, J. Lan, C. Zeng, Y. Liu, B. Zhan, S. Butt, Y.-H. Lin, and C.-W. Nan. "High performance oxides-based thermoelectric materials." In: *JOM* 67.1 (2015), pp. 211–221.

[29] T Okuda, K Nakanishi, S Miyasaka, and Y Tokura. "Large thermoelectric response of metallic perovskites: Sr 1- x La x TiO 3 (0<˜ x<˜ 0. 1)." In: *Physical Review B* 63.11 (2001), p. 113104.

[30] P. Jood, R. J. Mehta, Y. Zhang, G. Peleckis, X. Wang, R. W. Siegel, T. Borca-Tasciuc, S. X. Dou, and G. Ramanath. "Al-doped zinc oxide nanocomposites with enhanced thermoelectric properties." In: *Nano letters* 11.10 (2011), pp. 4337–4342.

[31] W. Shin and N. Murayama. "Li-doped nickel oxide as a thermoelectric material." In: *Japanese journal of applied physics* 38.11B (1999), p. L1336.

[32] Y.-H. Lin, C.-W. Nan, Y. Liu, J. Li, T Mizokawa, and Z. Shen. "High-Temperature Electrical Transport and Thermoelectric Power of Partially Substituted Ca3Co4O9-Based Ceramics." In: *Journal of the American Ceramic Society* 90.1 (2007), pp. 132–136.

[33] S. Obertelli, J. Cooper, and J. Tallon. "Systematics in the thermoelectric power of high-T c oxides." In: *Physical Review B* 46.22 (1992), p. 14928.

[34] D. Bérardan, E. Guilmeau, A. Maignan, and B. Raveau. ": Ge, a promising n-type thermoelectric oxide composite." In: *Solid State Communications* 146.1 (2008), pp. 97–101.

[35] M. Ohtaki, T. Tsubota, K. Eguchi, and H. Arai. "High-temperature thermoelectric properties of (Zn1- x Al x) O." In: *Journal of Applied Physics* 79.3 (1996), pp. 1816–1818.

[36] B. Cheng, H. Fang, J. Lan, Y. Liu, Y.-H. Lin, and C.-W. Nan. "Thermoelectric Performance of Zn and GeCo-Doped In2O3 Fine-Grained Ceramics by the Spark Plasma Sintering." In: *Journal of the American Ceramic Society* 94.8 (2011), pp. 2279–2281.

[37] J. Lan, Y.-H. Lin, Y. Liu, S. Xu, and C.-W. Nan. "High Thermoelectric Performance of Nanostructured In2O3-Based Ceramics." In: *Journal of the American Ceramic Society* 95.8 (2012), pp. 2465–2469.

[38] T. Maruyama and T. Tago. "Germanium-and silicon-doped indium-oxide thin films prepared by radio-frequency magnetron sputtering." In: *Applied physics letters* 64.11 (1994), pp. 1395–1397.

[39] N. Mitoma, S. Aikawa, X. Gao, T. Kizu, M. Shimizu, M.-F. Lin, T. Nabatame, and K. Tsukagoshi. "Stable amorphous In2O3-based thin-film transistors by incorporating SiO2 to suppress oxygen vacancies." In: *Applied Physics Letters* 104.10 (2014), p. 102103.

[40] N. Mitoma, S. Aikawa, W. Ou-Yang, X. Gao, T. Kizu, M.-F. Lin, A. Fujiwara, T. Nabatame, and K. Tsukagoshi. "Dopant selection for control of charge carrier density and mobility in amorphous indium oxide thin-film transistors: Comparison between Si-and W-dopants." In: *Applied Physics Letters* 106.4 (2015), p. 042106.

[41] S. Aikawa, T. Nabatame, and K. Tsukagoshi. "Effects of dopants in InOx-based amorphous oxide semiconductors for thin-film transistor applications." In: *Applied Physics Letters* 103.17 (2013), p. 172105.

[42] J.-W. Park, H. S. So, H.-M. Lee, H.-J. Kim, H.-K. Kim, and H. Lee. "Transition from a nanocrystalline phase to an amorphous phase in In-Si-O thin films: The correlation between the microstructure and the optical properties." In: *Journal of Applied Physics* 117.15 (2015), p. 155305.

[43] H.-M. Lee and H.-K. Kim. "Rapidly Thermal Annealed Si-Doped In2O3 Films for Organic Photovoltaics." In: *Journal of nanoscience and nanotechnology* 15.10 (2015), pp. 7748–7753.

[44] *Gwyddion – Free SPM data analysis software*. URL: http://gwyddion.net/.

[45] K. Wasa, I. Kanno, and H. Kotera. *Handbook of sputter deposition technology: fundamentals and applications for functional thin films, nano-materials and MEMS*. William Andrew, 2012.

[46] Y.-r. Luo and J. Kerr. "Bond dissociation energies." In: *CRC Handbook of Chemistry and Physics* 89 (2012).

[47] S. Berg and T. Nyberg. "Fundamental understanding and modeling of reactive sputtering processes." In: *Thin solid films* 476.2 (2005), pp. 215–230.

[48] Q. Song, B. Wu, B. Xie, F. Huang, M. Li, H. Wang, Y. Jiang, and Y. Song. "Resputtering of zinc oxide films prepared by radical assisted sputtering." In: *Journal of applied physics* 105.4 (2009), p. 044509.

[49] K Sreenivas, T Sudersena Rao, A. Mansingh, and S. Chandra. "Preparation and characterization of rf sputtered indium tin oxide films." In: *Journal of Applied Physics* 57.2 (1985), pp. 384–392.

[50] Y. Matsuda, Y. Yamori, M. Muta, S. Ohgushi, and H. Fujiyama. "Relation between plasma parameters and film properties in DC reactive magnetron sputtering of indium-tin-oxide." In: *Japanese journal of applied physics* 36.7S (1997), p. 4922.

[51] L Kerkache, A Layadi, and A Mosser. "Effect of oxygen partial pressure on the structural and optical properties of dc sputtered ITO thin films." In: *journal of Alloys and Compounds* 485.1 (2009), pp. 46–50.

[52] G. Li, J Zhou, Y. Huang, M Yang, J. Feng, and Q Zhang. "Indium zinc oxide semiconductor thin films deposited by dc magnetron sputtering at room temperature." In: *Vacuum* 85.1 (2010), pp. 22–25.

[53] N. Mitoma, B. Da, H. Yoshikawa, T. Nabatame, M. Takahashi, K. Ito, T. Kizu, A. Fujiwara, and K. Tsukagoshi. "Phase transitions from semiconductive amorphous to conductive polycrystalline in indium silicon oxide thin films." In: *Applied Physics Letters* 109.22 (2016), p. 221903.

[54] R. D. Shannon. "Revised effective ionic radii and systematic studies of interatomic distances in halides and chalcogenides." In: *Acta crystallographica section A: crystal physics, diffraction, theoretical and general crystallography* 32.5 (1976), pp. 751–767.

[55] L Kerkache, A Layadi, E Dogheche, and D Remiens. "Physical properties of RF sputtered ITO thin films and annealing effect." In: *Journal of Physics D: Applied Physics* 39.1 (2005), p. 184.

[56] J.-A. Jeong, Y.-S. Park, and H.-K. Kim. "Comparison of electrical, optical, structural, and interface properties of IZO-Ag-IZO and IZO-Au-IZO multilayer electrodes for organic photovoltaics." In: *Journal of Applied Physics* 107.2 (2010), p. 023111.

[57] A. Patterson. "The Scherrer formula for X-ray particle size determination." In: *Physical review* 56.10 (1939), p. 978.

[58] H. Guo, K. Zhang, X. Jia, C. Ma, N. Yuan, and J. Ding. "Effect of ITO film deposition conditions on ITO and CdS films of semiconductor solar cells." In: *Optik-International Journal for Light and Electron Optics* 140 (2017), pp. 322–330.

[59] D.-Y. Cho, Y.-H. Shin, and H.-K. Kim. "Highly transparent Si-doped In 2 O 3 films prepared on PET substrate using roll-to-roll sputtering." In: *Surface and Coatings Technology* 259 (2014), pp. 109–112.

[60] E.-G. Chong, Y.-S. Chun, S.-H. Kim, and S.-Y. Lee. "Effect of oxygen on the threshold voltage of a-IGZO TFT." In: *Journal of Electrical Engineering and Technology* 6.4 (2011), pp. 539–542.

[61] A. Suresh, P. Gollakota, P. Wellenius, A. Dhawan, and J. F. Muth. "Transparent, high mobility InGaZnO thin films deposited by PLD." In: *Thin Solid Films* 516.7 (2008), pp. 1326–1329.

[62] E. Chong, Y. S. Chun, and S. Y. Lee. "Amorphous silicon–indium–zinc oxide semiconductor thin film transistors processed below 150 C." In: *Applied Physics Letters* 97.10 (2010), p. 102102.

[63] S. Wen, G Campet, J Portier, G Couturier, and J. Goodenough. "Correlations between the electronic properties of doped indium oxide ceramics and the nature of the doping element." In: *Materials Science and Engineering: B* 14.1 (1992), pp. 115–119.

[64] A. J. Leenheer, J. D. Perkins, M. F. Van Hest, J. J. Berry, R. P. O'Hayre, and D. S. Ginley. "General mobility and carrier concentration relationship in transparent amorphous indium zinc oxide films." In: *Physical Review B* 77.11 (2008), p. 115215.

[65] C Guillén and J Herrero. "Structure, optical, and electrical properties of indium tin oxide thin films prepared by sputtering at room temperature and annealed in air or nitrogen." In: *Journal of applied physics* 101.7 (2007), p. 073514.

[66] K.-H. Choi, J.-A. Jeong, and H.-K. Kim. "Dependence of electrical, optical, and structural properties on the thickness of IZTO thin films grown by linear facing target sputtering for organic solar cells." In: *Solar Energy Materials and Solar Cells* 94.10 (2010), pp. 1822–1830.

[67] L Fang, X. Yang, L. Peng, K Zhou, F Wu, Q. Huang, and C. Kong. "Thermoelectric and magnetothermoelectric properties of In-doped nano-ZnO thin films prepared by RF magnetron sputtering." In: *Journal of superconductivity and novel magnetism* 23.6 (2010), pp. 889–892.

[68] Y. Chen, H. Jiang, S. Jiang, X. Liu, W. Zhang, and Q. Zhang. "Influence of annealing temperature on the microstructure and electrical properties of indium tin oxide thin films." In: *Acta Metallurgica Sinica (English Letters)* 27.2 (2014), pp. 368–372.

[69] N. Preissler, O. Bierwagen, A. T. Ramu, and J. S. Speck. "Electrical transport, electrothermal transport, and effective electron mass in single-crystalline In 2 O 3 films." In: *Physical Review B* 88.8 (2013), p. 085305.

[70] J.-J. Lin and Z.-Q. Li. "Electronic conduction properties of indium tin oxide: single-particle and many-body transport." In: *Journal of Physics: Condensed Matter* 26.34 (2014), p. 343201.

[71] J. Byeon, S. Kim, J.-H. Lim, J. Y. Song, S. H. Park, and P. Song. "Thermoelectric and electrical properties of micro-quantity Sn-doped amorphous indium–zinc oxide thin films." In: *Japanese Journal of Applied Physics* 56.1 (2016), p. 010304.

[72] Y. Fujimoto, M. Uenuma, Y. Ishikawa, and Y. Uraoka. "Thermoelectric Devices Fabricated Using Amorphous Indium Gallium Zinc Oxide." In: *ECS Transactions* 75.10 (2016), pp. 213–216.

[73] J. Lofy and L. Bell. "Thermoelectrics for environmental control in automobiles." In: *Thermoelectrics, 2002. Proceedings ICT'02. Twenty-First International Conference on Thermoelectrics*. IEEE. 2002, pp. 471–476.

[74] K Matsubara. "Development of a high efficient thermoelectric stack for a waste exhaust heat recovery of vehicles." In: *Thermoelectrics, 2002. Proceedings ICT'02. Twenty-First International Conference on*. IEEE. 2002, pp. 418–423.

[75] L. Chen, F. Meng, and F. Sun. "Thermodynamic analyses and optimization for thermoelectric devices: The state of the arts." In: *Science China Technological Sciences* 59.3 (2016), pp. 442–455. ISSN: 1869-1900. DOI: 10.1007/s11431-015-5970-5. URL: https://doi.org/10.1007/s11431-015-5970-5.

Appendix A

Thermoelectric effects

Besides the Seebeck effect, there are two more effects which are described below. In addition, is also presented the relation between the thermoelectric effects by the Kelvin relation.

Peltier Effect

J. Peltier discovered the second effect when he realised that if a current flows through a thermocouple, then a small heating appears at one junction and a cooling effect occurs at the other. On another words, a temperature gradient is established when a current flows through the material [9]. Therefore, the differential Peltier coefficient can be defined as

$$\pi_{ab} = \frac{q}{I} \tag{A.1}$$

where q is the rate of heating or cooling at each junction and I is the electric current. This coefficient, in V, is positive if the electric current enters at the heated junction and leaves at the cooled junction [9].

This effect can be demonstrated by connecting an external emf source to the open ends of the thermocouple [9].

Thomson Effect

The last effect was discovered several years later by W. Thomson when he related the rate of reversible heating or cooling due to an electric current flow, in a conductor, produced by a temperature difference. The differential Thomson coefficient is given by

$$\tau_{ab} = \frac{q}{I\Delta T} \tag{A.2}$$

where τ is the Thomson coefficient in V/K [9].

Kelvin relation

The previous coefficients were defined for a pair of conductors, and therefore they are assigned as differential coefficients. It would be of simpler practice if the coefficient could be assigned to a only one material. The conversion of differential coefficients into absolute can be made as long as the second material used is a superconductor (have zero absolute coefficients). Metal lead is a reference material for determining the absolute coefficients [9].

Between the Peltier and the Seebeck coefficients, the later is much simpler to measure [12]. One of the Kelvin relations simplifies the quantification of the Peltier coefficient by relating it to

the Seebeck coefficient. As a consequence of what was previously said for absolute coefficients, the first Kelvin relation can be defined as

$$\pi = ST \tag{A.3}$$

The remaining Kelvin relation combines the Seebeck coefficient and the Thomson coefficient, as described by the following

$$\tau = T\frac{\mathrm{d}S}{\mathrm{d}T} \tag{A.4}$$

Thus, if the absolute Seebeck coefficient of a material at low temperatures is determined by connecting it to superconductor, one can then use equation A.4 to find the value at higher temperatures after measuring the Thomson coefficient. This procedure has been carried out for metal lead, which may be used as a reference material when determining the absolute coefficients for other substances.

Applications

Thermoelectric devices can be applied to cooling or power generation. However, owing to a low efficiency (less than 6% [15]) they only find applications at a small scale. Still, some advantages over conventional technologies can be announced: absence of moving parts, reliability, durability, scalability, little mantainance, and no production of toxic pollutants [8].

Some of the practical applications of power generation can be found in aerospace applications, waste heat recovery for vehicles and industries [73, 74], medical services, and for electronic devices [8]. Cooling can be used for small scale refrigeration (figure A.1), detectors, and optoelectronics [10].

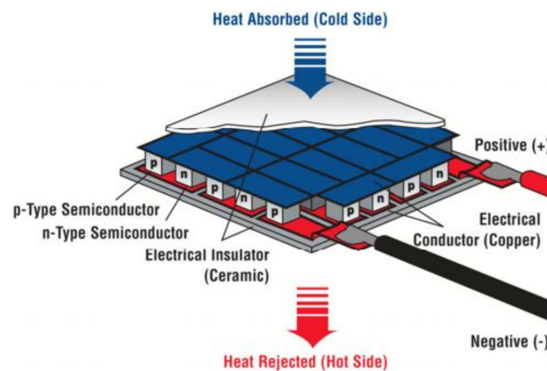

Figure A.1: Illustration of a Peltier module. From [75]

Appendix B

Structural characterisation

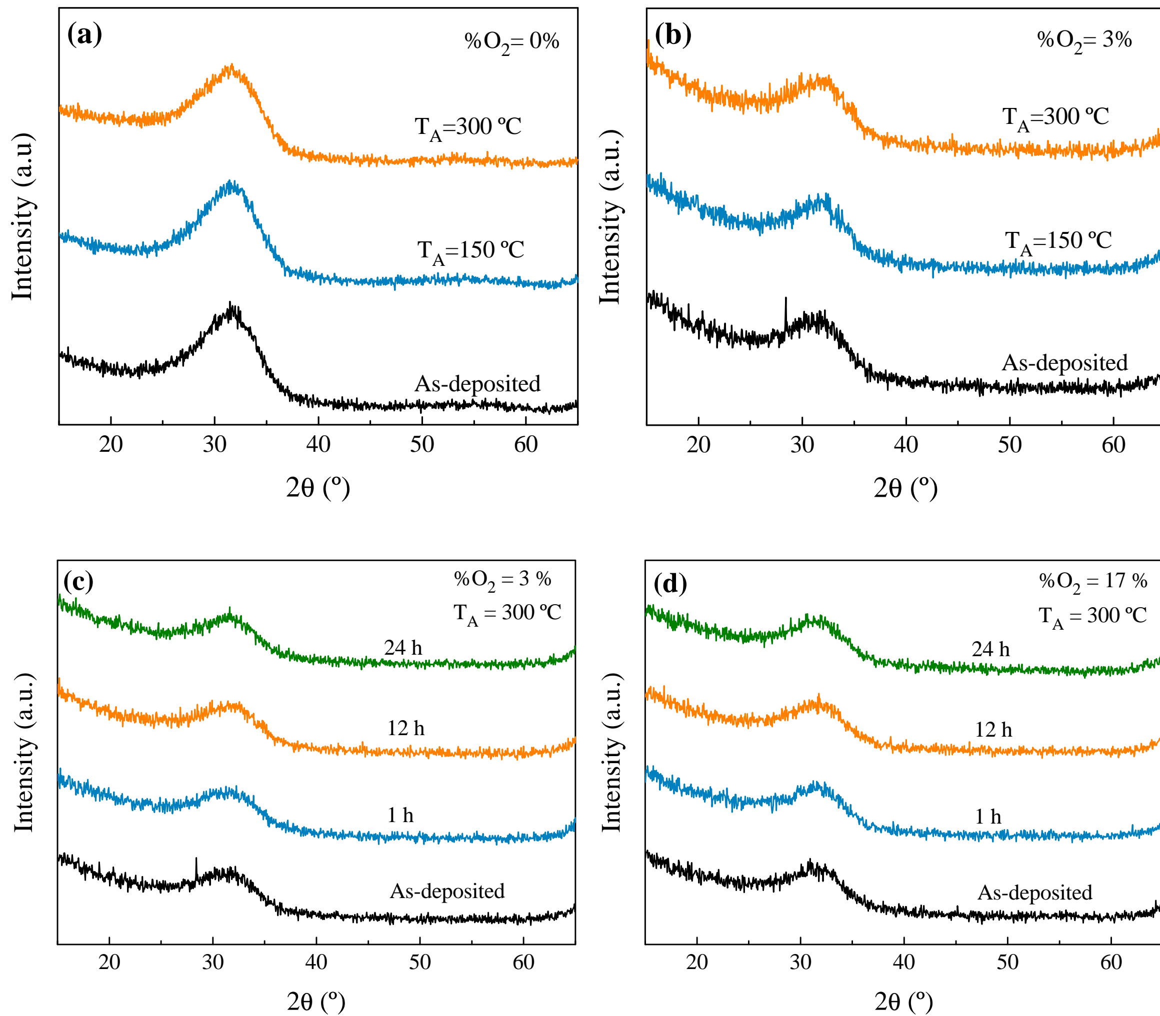

Figure B.1: Structure of ISO thin films annealed at different temperatures a) $\%O_2 = 0\%$, b) $\%O_2 = 3\%$ and at different annealing times c) $\%O_2 = 3\%$, d) $\%O_2 = 17\%$

Appendix C

Morphological characterisation

Surface morphology is depicted in figures C.1 and C.2 for annealed ISO films deposited under $\%O_2$ of 0 % and 17 %.

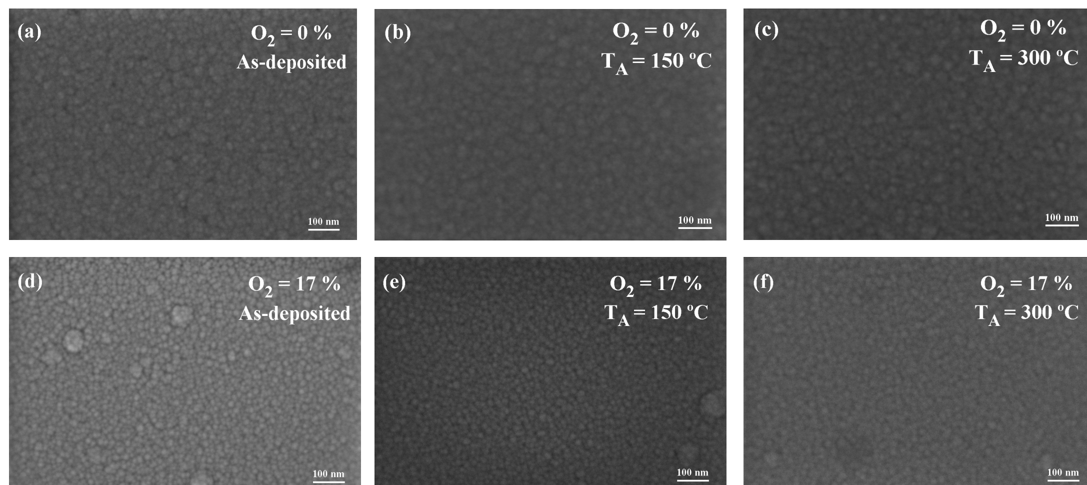

Figure C.1: Influence of different annealing temperatures on surface morphology for films deposited with (a) 0 % and (d) 17 % of $\%O_2$ and annealed at (b), (e) 150 ºC and (c), (f) 300 ºC. The SEM images for films deposited under 3 % of oxygen showed very similar results to films deposited under 17 %.

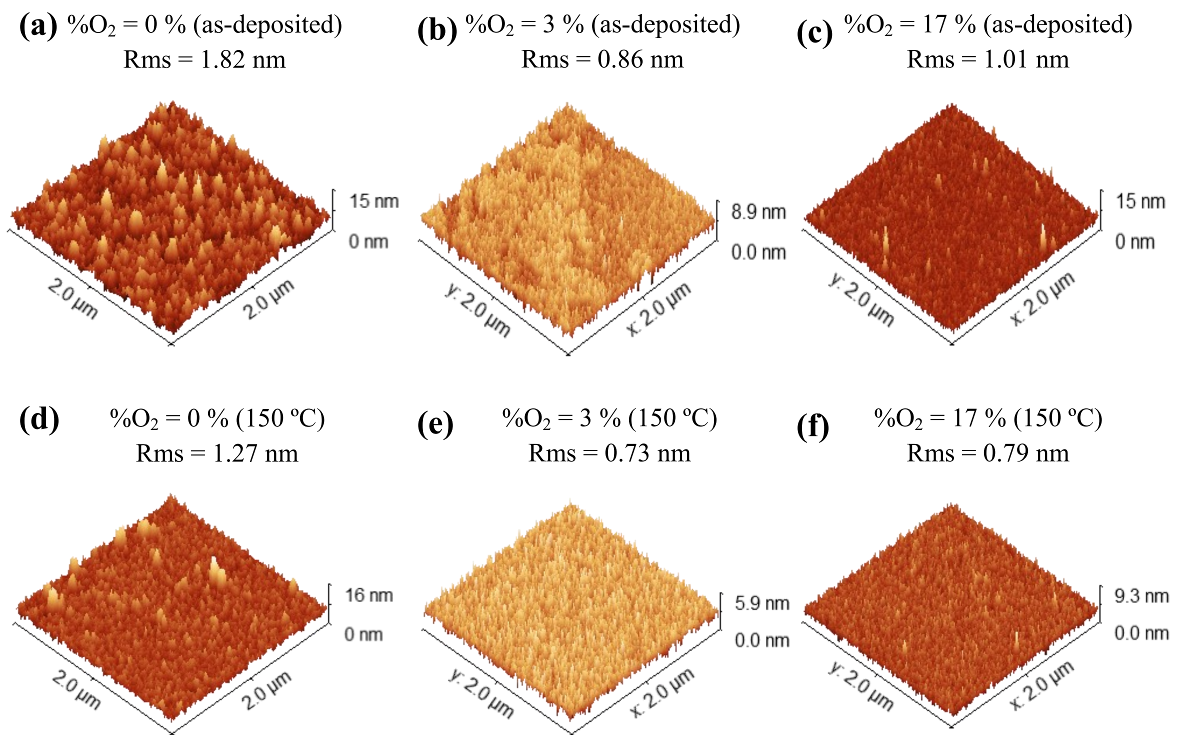

Figure C.2: AFM images for (a)-(c) as-deposited and (d)-(f) annealed at 150 ºC ISO thin films deposited under different sputtering gas compositions.

Appendix D

Optical characterisation

Optical transmittance and absorbance for different ISO thin films are presented in the following images. Thin films prepared under 3 % and 17 % of oxygen show very similar results. Additionally, no significant difference is observed between as-deposited and annealed films at 150 ºC.

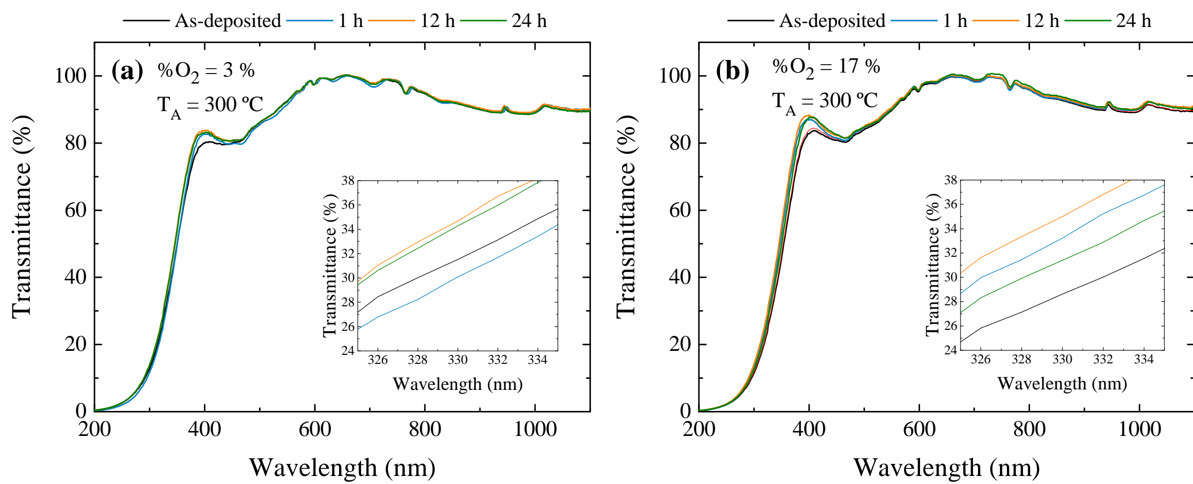

Figure D.1: Transmittance for films prepared with $\%O_2$ of (a) 3 % and (b) 17 % and annealed at 300 ºC for different periods. The inset explores the difference between each curve.

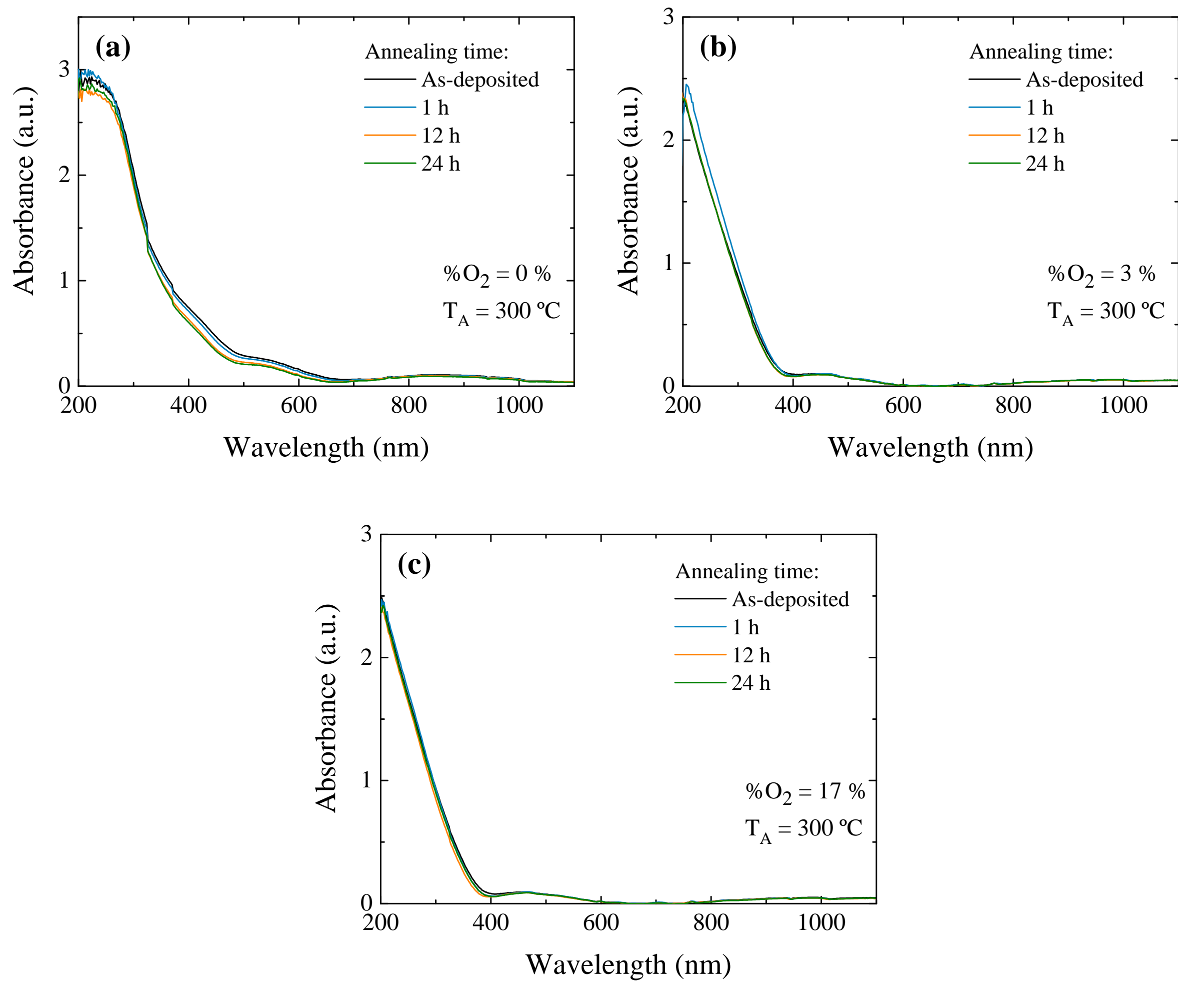

Figure D.2: Absorbance for films prepared with different %O_2 of (a) 0 %, (b) 3%, and (c) 17 % and annealed at 300 ºC for different periods. Thin films with 3 % and 17 % of oxygen used during deposition have the same optical absorbance.

Appendix E

Relative Seebeck coefficient determination

Illustration of the used slope method for relative Seebeck coefficient determination.

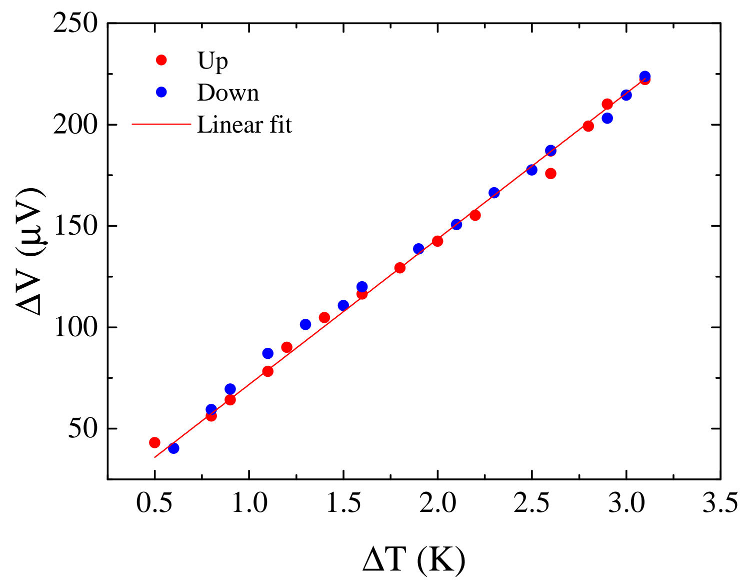

Figure E.1: Slope method for determination of the relative Seebeck coefficient.